Coherent Perfect Absorption in Weyl Semimetals: A Path to Topologically Enhanced Light-Matter Interactions

Güneş Oktay* and Mehmet Ertan Indap†
Institute of Graduate Studies in Science, Istanbul University, Istanbul 34134, Türkiye

Mustafa Sarısaman‡
Department of Physics, Istanbul University, 34134, Vezneciler, Istanbul, Türkiye

This study explores the unique intersection of Topological Weyl Semimetals (TWS) and non-Hermitian physics, focusing on the potential of Coherent Perfect Absorbers (CPAs) in such materials, with the investigation based on the fact that CPA is viewed as time-reversed lasers. We introduce a theoretical model for TWS CPAs based on the transfer matrix method, demonstrating that topologically protected surface states lead to 12 distinct feasible CPA configurations characterized by quantized loss values. This study offers a novel approach to understanding self-dual spectral singularities in the context of TWS and examines the impact of the axion term on the system's scattering behavior. Our findings reveal how the Θ-term significantly affects the loss value and its topological quantization, triggering the Weyl transition which leads to the multi-fold branching of these singularities and results in stable CPA states. CPA action induces the formation of topologically protected circular Hall currents within the TWS. These results pave the way for designing efficient, tunable, and topologically protected devices within non-Hermitian systems.

PACS numbers: 02.40.Hw, 03.65.−w, 03.65.Nk, 03.65.Pm, 03.75.−b, 04.20.−q, 04.25.Nx, 04.30.−w, 11.80.−m
Keywords: Non-Hermitian Physics; Topological Material; Weyl Semimetal; Scattering Theory; Transfer Matrix; Self- Dual Spectral Singularity; CPA; Topological Photonics

INTRODUCTION

Topology is emerging as a distinct field within mathematics that studies geometric objects and their inherent properties, which remain unchanged under continuous deformations such as twisting or stretching, without breaking or altering their fundamental characteristics. Remarkably, this abstract mathematical concept has tangible counterparts in the physical world, with numerous potential applications in areas like quantum matter, photonics, and electronics [1, 2]. In recent years, topological materials have gained attention for their promising applications due to their unique electronic and mechanical properties, which stem from their non-trivial topological features [3–5]. As a result, extensive theoretical and experimental research is underway to expand and optimize their practical use [6–18]. Among these materials, semimetals—characterized by an electronic band structure lying between metals and non-metals—stand out. Unlike metals and semiconductors, semimetals feature a slight intersection between the valence and conduction bands at the Fermi energy level [8, 19–32].

Within the expanding domain of topological materials, Weyl semimetals are especially notable due to their exceptional electronic properties and rich topological characteristics [19–32, 36–50]. These materials are defined by the presence of Weyl nodes—specific points in momentum space where the conduction and valence bands converge, leading to phenomena like Fermi arcs and chiral anomalies [32, 51–57]. These materials offer a wide range of unique properties that make them highly promising for advanced applications in fields such as quantum computing, electronics, spintronics, thermoelectrics, and photonics [39, 43, 58–64]. As our understanding of these materials deepens and fabrication technologies improve, their applications are expected to broaden, opening new avenues for technological innovations.

In this study, we examine a Topological Weyl Semimetal (TWS) system and investigate the impact of non-Hermitian effects, particularly in the context of electromagnetic wave scattering, to identify novel types of topological Coherent Perfect Absorbers (CPAs) that have not been explored in existing literature[1]. Unlike traditional absorption mechanisms, CPA occurs when the material is precisely tuned to absorb all incoming light without reflection or transmission, offering a path to novel light manipulation and energy harvesting technologies. This material is classified as topological due to a phase transition, which introduces an axion term and imparts topological properties to the system

---

[1] An extensive and rapidly growing body of literature on CPA action can be found in references [65–94]. For applications of CPA in topological materials, see the references [95–102].

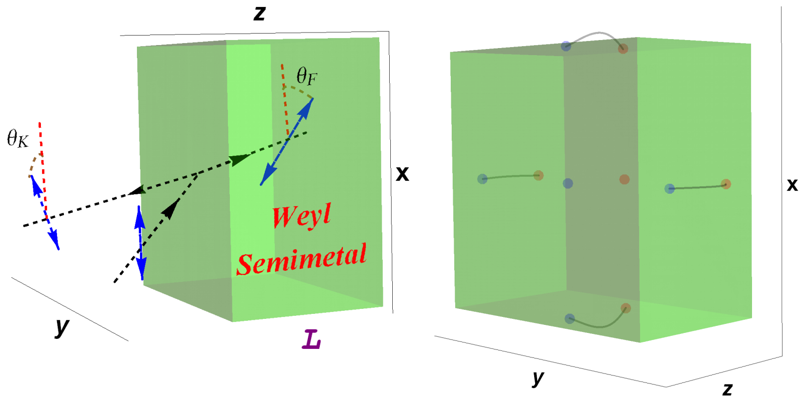

FIG. 1. (Color online) The TE mode configuration for the interaction of an electromagnetic wave with the Weyl semimetal slab. The wave is emitted on the slab by an angle θ which is measured from the normal to the surface, and the polarization direction is rotated by the Faraday angle θ_F inside and the Kerr angle θ_K outside the slab respectively. On the right panel, Fermi arcs due to Weyl nodes are presented.

[103, 104, 106]. While significant progress has been made in understanding its behavior, the optical interactions and full topological implications remain inadequately explored [29, 36–50]. This work aims to bridge this gap by investigating TWS materials in the context of CPA design. We propose a theoretical model for a TWS CPA using the transfer matrix method, demonstrating that the topological protection of surface states gives rise to 12 distinct types of topological CPAs. These types are characterized by quantized loss values necessary to satisfy the CPA condition, all while respecting the topological symmetries. Our system, as depicted in Fig. 1, consists of a TWS material with Weyl nodes aligned along the z-axis.

The non-Hermitian approach to topological materials has recently gained significant attention. Unlike traditional Hermitian systems, where the hermiticity guarantees probability conservation and yield real eigenvalues, non-Hermitian systems exhibit distinct phenomena, such as the coalescence of eigenstates at exceptional points and the emergence of robust edge states that are resistant to perturbations [107–124]. These systems modify the standard principles of quantum mechanics, leading to novel effects such as exceptional points, unidirectional light propagation, enhanced laser performance, and coherent perfect absorption (CPA) [66, 99, 125–137, 143–150]. The symmetry inherent in these systems enables the design of materials that are not only topologically protected but also capable of supporting unique physical phenomena, such as unidirectional light propagation and topologically protected lasing and CPA. For TWS materials, non-Hermitian exceptional points facilitate the stabilization of surface states that would typically be unstable in other non-Hermitian systems. This opens up new possibilities for controlling light-matter interactions, developing advanced optoelectronic devices, and realizing novel topological phases with potential applications in quantum information processing, sensing, and lasing.

In this paper, we construct a conceptual framework of a TWS CPA device by employing the transfer matrix approach in view of non-Hermitian physics. It is a well-known that the construction of a CPA depends on the identification of the self-dual spectral singularity points in the non-Hermitian system [99, 129, 131, 132, 136, 151].

Spectral singularities, including self-dual spectral singularities, represent a remarkable phenomenon where the density of states exhibits a peak of infinite height, and have become an essential focus in the study of non-Hermitian systems. These singularities are intimately linked to exceptional points, where eigenvalues and eigenvectors coalesce, and they manifest across a wide range of physical phenomena, from optics to quantum mechanics. In the context of optical systems, spectral singularities (and self-dual ones, in particular) arise in scattering scenarios, where the reflection and transmission amplitudes diverge for real values of the wave-vector k in the physical system [99, 125, 127–132, 136, 143, 151–153]. This divergence leads to the formation of zero-width resonances and the emergence of laser/CPA threshold states, characterized by purely outgoing or incoming waves [143]. Such behavior is a hallmark of non-Hermitian physics, distinguishing it from conventional lasers and CPAs. Recent years have seen substantial progress in uncovering new phenomena within non-Hermitian physics, with a growing body of studies exploring its rich and unexplored aspects [108, 113–124]. This field plays a crucial role in understanding the unique properties of topological materials [99, 126, 147, 148], forming the central motivation for our work. Investigating topological systems within the framework of non-Hermitian physics offers an innovative perspective, and the inclusion of Weyl semimetals in this context is opening up new avenues for designing CPAs with exceptional efficiency, tunability, and robustness, providing deeper insights into the interplay between symmetry, topology, and spectral properties.

We begin by introducing the fundamental concepts of Weyl semimetals, like Fermi arcs, Kerr and Faraday rotations, and dimensional enhancement, highlighting their unique topological properties. We then explore the concept of self-dual spectral singularities, examining their origins, implications, and manifestation within the context of TWS. By focusing on these self-dual singularities, we aim to uncover their influence on the electronic structure and physical properties of these materials. Through this analysis, we seek to demonstrate the potential of Weyl semimetals to exhibit novel spectral features, with important implications for future research and technological advancements in both topological and non-Hermitian systems.

The recent observation of Kerr and Faraday effects in Weyl semimetals cause an increment of the system's effective dimension, introducing additional computational challenges in structural analysis [126]. However, this complexity also provides valuable insights and enrichment into the underlying physics. Our study has uncovered new and previously unrecognized properties of TWS by investigating these intricate interactions. To tackle the challenges posed by these effects, we have structured our system in a way that results in a 4×4 transfer matrix due to the Kerr/Faraday effect. This leads to 12 distinct CPA configurations, which display topologically robust features. By generating waves in the transverse electric (TE) mode, we aim to explore the topological aspects of the system and gain a deeper understanding of its characteristics. The topological properties of such systems are known to be governed by the Θ-term [104, 105], where, in our case, the term corresponds to b, the distance between the Weyl nodes in the bulk structure.

To explore the influence of the Θ-term on the topological properties of the system, we will focus on analyzing the scattering behavior of TWS, identify self-dual spectral singularities, and examine how these singularities are affected by the Θ-term. Self-dual spectral singularities occur at points where the system's continuous spectrum exhibits unique and exceptional features [152, 153], which in turn lead to the formation of CPA. Therefore, the interaction between TWS and electromagnetic waves can be framed as a non-Hermitian scattering problem in the context of electromagnetic theory [126].

Our study is organized as follows: Initially, we computed the transfer matrix by solving Maxwell's equations, incorporating the axion term, for the TE mode configuration specific to a lossy Weyl semimetal. This transfer matrix enabled us to calculate the self-dual spectral singularities. In the final part of our analysis, we examined the impact of the Θ-term on these singularities by using TaAs material, which has been experimentally verified to support the Weyl semimetal phase [30, 154–161]. Our results provide novel insights into the understanding of CPA formation in TWS materials. We demonstrate that the Θ-term significantly reduces the system's loss value and leads to the topological quantization of the system, evident through the degeneration of the self-dual spectral singularity points. This finding is significant and is reported for the first time in the literature. At this point, we clearly show that the b-term plays a crucial role in the system's topological properties, triggering the Weyl transition at the self-dual spectral singularity points. Additionally, we determined the axion-induced current within the TWS medium, which exhibits cyclotron-like Hall current patterns with a topological origin confined to the xy-plane. These currents display distinct behaviors in the lossy TWS medium. Our study also reveals that 12 different topological CPA types can be generated due to the Kerr/Faraday effect in the TWS material, and it identifies the conditions under which these CPA configurations can exist.

TE MODE SOLUTION AND TRANSFER MATRIX

Consider a linear, homogeneous and planar TWS slab which consists of optically active loss component. Geometry of the slab is designed in such a way that an appropriate CPA can be constructed respecting the alignment of Weyl nodes along the z-axis as displayed in Fig. 1. TWS slab is described by the thickness L and a uniform complex refractive index $\mathfrak{n}$ which has a constant value within the TWS medium. Interaction of this slab with the electromagnetic waves is governed by the Maxwell's equations, which incorporate topological terms due to the magnetoelectric optical effects. Topological characteristics of the designed system arises from the alignment of Weyl nodes which determine the locations of fermi arcs on the corresponding surfaces of TWS slab. As depicted in Fig. 1, fermi arcs appear on surfaces along the z-axis. According to our optical design, Maxwell's equations are given by

$$\vec{\nabla}\cdot\vec{\mathcal{D}} = \rho(z) + \beta\,\vec{b}\cdot\vec{\mathcal{B}}, \qquad \vec{\nabla}\cdot\vec{\mathcal{B}} = 0, \tag{1}$$

$$\vec{\nabla}\times\vec{\mathcal{H}} - \partial_t\vec{\mathcal{D}} = \vec{\mathcal{J}}(z) - \beta\,\vec{b}\times\vec{\mathcal{E}}, \qquad \partial_t\vec{\mathcal{B}} + \vec{\nabla}\times\vec{\mathcal{E}} = \vec{0}, \tag{2}$$

where $\beta := 2\alpha/\pi Z_0$ is a constant, $\alpha := e^2/2\varepsilon_0 hc$ is the fine structure constant, $Z_0 := \sqrt{\mu_0/\varepsilon_0}$ is the vacuum impedance, e is the charge of an electron and $c := 1/\sqrt{\varepsilon_0\mu_0}$ is the speed of light in vacuum. The vector $\vec{b}$ denotes the distance between two Weyl nodes which are aligned in z-direction and is given explicitly by $\vec{b}(z) = b\hat{e}_z$ for $0 < z < L$. Notice that $\vec{\mathcal{E}}$ and $\vec{\mathcal{B}}$ represent the electric and magnetic fields respectively, and are expressed by $\vec{\mathcal{D}}$ and $\vec{\mathcal{H}}$ fields via the following constitutive relations

$$\vec{\mathcal{D}} := \tilde{\varepsilon}\,\vec{\mathcal{E}}, \qquad \vec{\mathcal{B}} := \tilde{\mu}\vec{\mathcal{H}},$$

where $\tilde{\varepsilon}$ and $\tilde{\mu}$ are respectively the permittivity and permeability of the relevant environment in which electromagnetic wave propagates. These are described by $\tilde{\varepsilon} := \varepsilon_0\varepsilon$ and $\tilde{\mu} := \mu_0\mu$ respectively in terms of vacuum permittivity and permeability, where we defined $\varepsilon(z) := \varepsilon_b + \frac{i\sigma_{yy}}{\varepsilon_0\omega}$ and $\mu(z) := 1 + \chi_m$ for $z \in [0, L]$. Here, ε_b is the bound charge contribution, χ_m is the magnetic susceptibility of TWS provided that it exhibits a magnetic characteristics. In this paper, we assume that TWS is endowed with a rather weak magnetism such that we may ignore it [2]. Notice that $\mathfrak{n}^2 := \varepsilon\mu$ within the slab, where $\mathfrak{n}$ corresponds to the complex-valued refractive index of the TWS.

Electric current density that appears in Maxwell equations is given by $\vec{\mathcal{J}}(z) := \sigma(z)\vec{\mathcal{E}}(z)$ for $z = 0$ and L, where $\sigma(z)$ is the surface conductivity on the corresponding surfaces of TWS. Formally, we can express the surface current $\vec{\mathcal{J}}^s$ in tensorial notation as $\vec{\mathcal{J}}^s_\alpha = \sigma^s_{\alpha\beta}\vec{E}_\beta$, where conductivities $\sigma^s_{\alpha\beta}$ are specified to be

$$\sigma^s_{yy} = \frac{e^2 k_c}{3\pi h\hat{\omega}_c}\left\{1 - i\left[\hat{\omega}_c^2 + \ln\left|1 - \hat{\omega}_c^2\right|\right]\right\}, \tag{3}$$

$$\sigma^s_{yx} = \frac{e^2 b}{\pi h} + \frac{\alpha c}{3\pi v_F}\ln\left|1 - \hat{\omega}_c^2\right|, \tag{4}$$

where $\hat{\omega}_c := 2\omega_c/\omega$, $\omega_c := v_F k_c$, v_F is the Fermi velocity, k_c is the momentum cut-off and $k \le k_c$. We notice that the component σ^s_{yx} in (4) conducts the Kerr and Faraday rotations inside and outside the TWS slab. Besides, we realize that there is an accompanying free surface charges to the surface currents, which are directly related to each other by the continuity equation,

$$\vec{\nabla}\cdot\vec{\mathcal{J}}^s + \partial_t\rho^s(z) = 0. \tag{5}$$

We emphasize that free charges and currents are formed only on the surfaces of the TWS slab on which the incident wave emerges and no fermi arcs are present. This makes TWS slab a conductor at surfaces, and a semimetal inside the TWS material due to the induced current $\vec{\mathcal{J}}_\theta = -\beta\,\vec{b}\times\vec{\mathcal{E}}$ that appear in Maxwell's third equation.

Now, we investigate TE mode solutions of Maxwell equations and consider obliquely incident time harmonic electromagnetic waves in the form, see Fig. 1

$$\vec{E}(\vec{r}) = \mathscr{E}(z)e^{ik_x x}\hat{e}_y, \tag{6}$$

In this expression, we adopt the cartesian coordinates $x, y,$ and$z$ with corresponding unit vectors $\hat{e}_j$ with $j = x, y$ and z. k_j is the components of the wavevector along the j-axis, i.e. $k_x = k\,\sin\theta$, $k_z = k\,\cos\theta$ and $\theta \in [-90^\circ, 90^\circ]$. We point out that polarization direction of the incident wave is twisted when it is reflected and refracted at the interface of TWS. Reflected waves leads to the Kerr rotation, and the refracted waves to the Faraday rotation within the slab, see Fig. 1.

Maxwell equations in (1) and (2) give rise to the 3-dimensional Helmholtz equation associated with the TE mode states and the corresponding magnetic field $\vec{H}$ as follows

$$\left[\nabla^2 + k^2\varepsilon(z)\mu(z)\right]\vec{E} - i\beta k Z_0\vec{b}\times\vec{E} = 0, \tag{7}$$

$$\vec{H} = -\frac{i}{kZ_0\mu(z)}\vec{\nabla}\times\vec{E}, \tag{8}$$

These are in fact coupled equations when twisted waves arise. In view of Kerr and Faraday rotations together with the formal equivalence between Helmholtz and Schrödinger equations, it is immediate that Eqs. (7) and (8) yield the following uncoupled equations

$$-\psi''_\pm + v_\pm(\mathbf{z})\psi_\pm = \mathfrak{K}^2\psi_\pm, \tag{9}$$

---

[2] For the sake of full discussion, we keep its presence till the end.

for the potentials given by $v_{\pm}(\mathbf{z}) = \mathfrak{K}^2\mathfrak{z}_{\pm}(\mathbf{z})$, where $\mathfrak{z}_{\pm}(\mathbf{z})$ is defined to be

$$\mathfrak{z}_{\pm}(\mathbf{z}) := \mathfrak{z}(\mathbf{z}) \pm \frac{2\alpha L b(\mathbf{z})}{\pi\mathfrak{K}\cos\theta}, \qquad \mathfrak{z}(\mathbf{z}) := \left\{\begin{array}{ll} \tilde{\mathfrak{n}}^2 & \text{for} \quad \mathbf{z}\in[0,1], \\ 1 & \quad\text{otherwise}\end{array}\right., \qquad \tilde{\mathfrak{n}} := \sec\theta\sqrt{\mathfrak{n}^2-\sin^2\theta}. \tag{10}$$

In these equations, we make use of the following scaled variables for the convenience of the subsequent expressions

$$\mathbf{x} := \frac{x}{L}, \qquad \mathbf{z} := \frac{z}{L}, \qquad \mathfrak{K} := Lk_z = kL\cos\theta. \tag{11}$$

We observe that $\psi_{\pm}$ corresponds to a set of solutions which give rise to what we call as plus and minus modes respectively. Thus, it is immediate to see that each mode possesses its own refractive index within the TWS slab, i.e. $\tilde{\mathfrak{n}}_{\pm}$ which are given by

$$\tilde{\mathfrak{n}}_{\pm} = \sqrt{\tilde{\mathfrak{n}}^2 \pm 2\alpha bL/\pi\mathfrak{K}\cos\theta}. \tag{12}$$

These are in fact effective refractive indices which produce the birefringence effect for the TWS slab. This phenomenon occurs because of the presence of the term b in (12). Therefore, one computes the electric field $\vec{E}$ and magnetic field $\vec{H}$ in components as in Table I, where the quantities $\mathcal{F}_{\pm}$ and $\mathcal{G}_{\pm}$ are defined in different regions of optical TWS slab system by

Components of $\vec{E}$-field	Components of $\vec{H}$-field
$E_x = \frac{(\mathcal{F}_+ + \mathcal{G}_+)}{2}\, e^{i\mathfrak{K}\mathbf{x}\tan\theta}$	$H_x = \frac{i\cos\theta}{2Z_0}\left[\sqrt{\mathfrak{z}_+}\mathcal{F}_- - \sqrt{\mathfrak{z}_-}\mathcal{G}_-\right] e^{i\mathfrak{K}\mathbf{x}\tan\theta}$
$E_y = \frac{-i(\mathcal{F}_+ - \mathcal{G}_+)}{2}\, e^{i\mathfrak{K}\mathbf{x}\tan\theta}$	$H_y = \frac{\cos\theta}{2Z_0\mu}\left[\sqrt{\mathfrak{z}_+}\mathcal{F}_- + \sqrt{\mathfrak{z}_-}\mathcal{G}_-\right] e^{i\mathfrak{K}\mathbf{x}\tan\theta}$
$E_z = 0$	$H_z = -\frac{i\sin\theta}{2Z_0}\left[\mathcal{F}_+ - \mathcal{G}_+\right] e^{i\mathfrak{K}\mathbf{x}\tan\theta}$

TABLE I. Components of $\vec{E}$ and $\vec{H}$ fields existing inside and outside the TWS slab.

$$\mathcal{F}_{\pm} := \left\{\begin{array}{ll} A_1^{(+)}\, e^{i\mathfrak{K}\mathbf{z}} \pm C_1^{(+)}\, e^{-i\mathfrak{K}\mathbf{z}} & \text{for} \;\; \mathbf{z}<0, \\ B_1^{(+)}\, e^{i\mathfrak{K}_+\mathbf{z}} \pm B_2^{(+)}\, e^{-i\mathfrak{K}_+\mathbf{z}} & \text{for} \;\; 0<\mathbf{z}<1, \\ A_2^{(+)}\, e^{i\mathfrak{K}\mathbf{z}} \pm C_2^{(+)}\, e^{-i\mathfrak{K}\mathbf{z}} & \text{for} \;\; \mathbf{z}>1. \end{array}\right. \qquad \mathcal{G}_{\pm} := \left\{\begin{array}{ll} A_1^{(-)}\, e^{i\mathfrak{K}\mathbf{z}} \pm C_1^{(-)}\, e^{-i\mathfrak{K}\mathbf{z}} & \text{for} \;\; \mathbf{z}<0, \\ B_1^{(-)}\, e^{i\mathfrak{K}_-\mathbf{z}} \pm B_2^{(-)}\, e^{-i\mathfrak{K}_-\mathbf{z}} & \text{for} \;\; 0<\mathbf{z}<1, \\ A_2^{(-)}\, e^{i\mathfrak{K}\mathbf{z}} \pm C_2^{(-)}\, e^{-i\mathfrak{K}\mathbf{z}} & \text{for} \;\; \mathbf{z}>1. \end{array}\right.$$

Here we introduced the quantity $\mathfrak{K}_j$ as follows

$$\mathfrak{K}_j := \mathfrak{K}\tilde{\mathfrak{n}}_j. \tag{13}$$

$\mathfrak{K}$-dependent complex coefficients $A_j^{(\pm)}, B_j^{(\pm)}$ and $C_j^{(\pm)}$ are related to each other via appropriate boundary conditions present in our configuration of the TWS slab system. See Appendix for the associated boundary conditions. Therefore, transfer matrix can be constructed as follows

$$\left(\begin{array}{c}\mathbf{A}_2\\ \mathbf{C}_2\end{array}\right) = \mathbb{M}(\mathfrak{K})\left(\begin{array}{c}\mathbf{A}_1\\ \mathbf{C}_1\end{array}\right),$$

where $\mathbf{A}_j$ and $\mathbf{C}_j$ with $j=1,2$ are the column matrices which represent the coefficients of right and left moving waves outside the TWS slab, and are given by

$$\mathbf{A}_j = \left(\begin{array}{c}A_j^{(+)}\\ A_j^{(-)}\end{array}\right), \qquad \mathbf{C}_j = \left(\begin{array}{c}C_j^{(+)}\\ C_j^{(-)}\end{array}\right),$$

and $\mathbb{M}(\mathfrak{K})$ is the 4×4 transfer matrix [143] which is expressed by 2×2 matrix-valued reflection and transmission amplitudes,

$$\mathbb{M}(\mathfrak{K}) = \left(\begin{array}{cc}\mathbf{T}^l - \mathbf{R}^l\mathbf{T}^{-r}\mathbf{R}^r & \mathbf{R}^r\mathbf{T}^{-r}\\ -\mathbf{T}^{-r}\mathbf{R}^l & \mathbf{T}^{-r}\end{array}\right), \tag{14}$$

where $\mathbf{T}^{l/r}$ and $\mathbf{R}^{l/r}$ are the left/right transmission and reflection amplitudes, respectively. We see that transfer matrix (14) reveals all the information about the reflection and transmission properties of the TWS optical system.

CPA is obtained by the self-dual spectral singularity condition given by the zeros of certain components of the transfer matrix $\mathbb{M}$ corresponding to the real $\mathfrak{K}$ values.Thus, we attain purely incoming waves at self-dual spectral singularity points. This approach notably incorporates all the parameters of the TWS system into the transfer matrix, which is embedded within the reflection and transmission amplitudes. By properly managing these parameters, we are able to manipulate the transfer matrix to achieve the desired results. To improve the applicability of this method, we will decompose the transfer matrix, highlighting a particularly useful decomposition,

$$\mathbb{M} = \mathbb{K}^{-1}\mathbb{S}^{-1}\mathbb{L}\,\mathbb{S}. \tag{15}$$

Here, $\mathbb{K}$ and $\mathbb{L}$ matrices represent the phases depending on the refractive indices $\tilde{\mathfrak{n}}_{\pm}$, whereas $\mathbb{S}$ matrix serves as the characteristic matrix that demonstrates how the CPA environment depends on other parameters. These decomposition matrices are explicitly represented by the following expressions,

$$\mathbb{K} := \begin{pmatrix} e^{i\mathfrak{K}} & 0 & 0 & 0 \\ 0 & e^{i\mathfrak{K}} & 0 & 0 \\ 0 & 0 & e^{-i\mathfrak{K}} & 0 \\ 0 & 0 & 0 & e^{-i\mathfrak{K}} \end{pmatrix}, \qquad \mathbb{L} := \begin{pmatrix} e^{i\mathfrak{K}_+} & 0 & 0 & 0 \\ 0 & e^{-i\mathfrak{K}_+} & 0 & 0 \\ 0 & 0 & e^{i\mathfrak{K}_-} & 0 \\ 0 & 0 & 0 & e^{i\mathfrak{K}_-} \end{pmatrix},$$

$$\mathbb{S} := \begin{pmatrix} \tilde{\mathfrak{n}}_+ + \mu(1+\sigma_+) & -\mu\sigma_- & \tilde{\mathfrak{n}}_+ - \mu(1-\sigma_+) & -\mu\sigma_- \\ \tilde{\mathfrak{n}}_+ - \mu(1+\sigma_+) & \mu\sigma_- & \tilde{\mathfrak{n}}_+ + \mu(1-\sigma_+) & \mu\sigma_- \\ -\mu\sigma_+ & \tilde{\mathfrak{n}}_- + \mu(1+\sigma_-) & -\mu\sigma_+ & \tilde{\mathfrak{n}}_- - \mu(1-\sigma_-) \\ \mu\sigma_+ & \tilde{\mathfrak{n}}_- - \mu(1+\sigma_-) & \mu\sigma_+ & \tilde{\mathfrak{n}}_- + \mu(1-\sigma_-) \end{pmatrix}.$$

The decomposition of the incoming wave within the material medium into two distinct modes (and refractive indices $\tilde{\mathfrak{n}}_{\pm}$) due to the birefringence effect offers various possibilities for the type of CPA that can be realized. This result is indeed noteworthy. Initially, a one-dimensional environment acquires a topological character owing to its axionic properties, thereby increasing the system's dimensionality and creating a situation similar to a two-dimensional scattering medium. This paves the way for the formation of CPA types that have not been observed in any material before. In summary, Table II provides a comprehensive list of the CPA types that can be obtained from such a material, along with the corresponding configurations generated by these different types of CPA.

Table II presents 12 distinct CPA types that can be achieved based on the wave type incident from the right and left sides of a TWS slab. While the total number of potential CPA configurations is 16, four of these are not permissible. To highlight the uniqueness of each CPA configuration, we have assigned different colors to the various types in the table. The final column in Table II outlines the conditions for each CPA type, which correspond to the real zeros of the relevant components of the transfer matrix. It is important to note that all listed conditions must be satisfied simultaneously in order to obtain the specified CPA type.

Now we define continuous functions $\{\alpha_{ij}^{(\ell)}, \beta_{ij}^{(\ell)}, \gamma_{ij}^{(\ell)}, \zeta_{ij}^{(\ell)}\}$: $\mathbb{C} \to \mathbb{C}$, which are specified by

$$\begin{aligned}
\alpha_{ij}^{(\ell)} &:= \ell\cos\mathfrak{K}_i - \mathbf{b}_j\sin\mathfrak{K}_j + \mathbf{c}_i\sin\mathfrak{K}_i, \\
\beta_{ij}^{(\ell)} &:= \left[\frac{1}{2}(\cos\mathfrak{K}_j - \cos\mathfrak{K}_i) + \mathbf{a}_i^{(\ell)}\sin\mathfrak{K}_i + \mathbf{a}_j^{(-\ell)}\sin\mathfrak{K}_j\right]\sigma_j, \\
\gamma_{ij}^{(\ell)} &:= -\mathbf{b}_j\sin\mathfrak{K}_j + \mathbf{d}_i^{(\ell)}\sin\mathfrak{K}_i, \\
\zeta_{ij}^{(\ell)} &:= \left[\frac{1}{2}(\cos\mathfrak{K}_j - \cos\mathfrak{K}_i) + \mathbf{a}_i^{(\ell)}\sin\mathfrak{K}_i + \mathbf{a}_j^{(\ell)}\sin\mathfrak{K}_j\right]\sigma_j,
\end{aligned}$$

where the indices i, j and ℓ take values $+$ and $-$, such that complex-valued coefficients $\mathbf{a}_j^{(\ell)}$, $\mathbf{b}_j$, $\mathbf{c}_j$, and $\mathbf{d}_j^{(\ell)}$ are defined as follows[3]

$$\mathbf{a}_j^{(\ell)} := \frac{i\mu(\sigma_j - \ell)}{2\tilde{\mathfrak{n}}_j}, \quad \mathbf{b}_j := \frac{i\mu\,\sigma_+\sigma_-}{2\tilde{\mathfrak{n}}_j}, \quad \mathbf{c}_j := \frac{i[\tilde{\mathfrak{n}}_j^2 - \mu^2(\sigma_j^2 - 1)]}{2\mu\tilde{\mathfrak{n}}_j}, \quad \mathbf{d}_j^{(\ell)} := \frac{i[\tilde{\mathfrak{n}}_j^2 - \mu^2(\sigma_j - \ell)^2]}{2\mu\tilde{\mathfrak{n}}_j}. \tag{16}$$

---

[3] Note that the symbol 'i" used in these expressions represents the imaginary unit. The index 'i" in the discussions may be mistaken for the imaginary unit, so the reader should be attentive to this distinction.

Type of CPA	**Identification of CPA**	**Left Side**	**Right Side**	**Self – Dual SS Condition**
Type 1	Unidirectional CPA from Left [+ Mode]	$+$	**None**	$\mathbf{M}_{11} = \mathbf{M}_{21} = \mathbf{M}_{31} = \mathbf{M}_{41} = 0$
Type 2	Unidirectional CPA from Left [− Mode]	$-$	**None**	$\mathbf{M}_{12} = \mathbf{M}_{22} = \mathbf{M}_{32} = \mathbf{M}_{42} = 0$
Type 3	Unidirectional CPA from Left [Bimodal]	$+$ & $-$	**None**	$\mathbf{M}_{11} = \mathbf{M}_{21} = \mathbf{M}_{31} = \mathbf{M}_{41} = 0$ $\mathbf{M}_{12} = \mathbf{M}_{22} = \mathbf{M}_{32} = \mathbf{M}_{42} = 0$
Type 4	Bidirectional CPA [+ Mode]	$+$	$+$	$\mathbf{M}_{11} = \mathbf{M}_{21} = \mathbf{M}_{41} = 0$
Type 5	Bidirectional CPA [+ from Left, − from Right]	$+$	$-$	$\mathbf{M}_{11} = \mathbf{M}_{21} = \mathbf{M}_{31} = 0$
Type 6	Bidirectional CPA [− from Left, + from Right]	$-$	$+$	$\mathbf{M}_{12} = \mathbf{M}_{22} = \mathbf{M}_{42} = 0$
Type 7	Bidirectional CPA [− Mode]	$-$	$-$	$\mathbf{M}_{12} = \mathbf{M}_{22} = \mathbf{M}_{32} = 0$
Type 8	Bidirectional CPA [+ from Left, +&− from Right]	$+$	$+$ & $-$	$\mathbf{M}_{11} = \mathbf{M}_{21} = 0$
Type 9	Bidirectional CPA [− from Left, +&− from Right]	$-$	$+$ & $-$	$\mathbf{M}_{12} = \mathbf{M}_{22} = 0$
Type 10	Bidirectional CPA [+&− from Left, + from Right]	$+$ & $-$	$+$	$\mathbf{M}_{11} = \mathbf{M}_{12} = 0$ $\mathbf{M}_{21} = \mathbf{M}_{22} = 0$ $\mathbf{M}_{41} = \mathbf{M}_{42} = 0$
Type 11	Bidirectional CPA [+&− from Left, − from Right]	$+$ & $-$	$-$	$\mathbf{M}_{11} = \mathbf{M}_{12} = 0$ $\mathbf{M}_{21} = \mathbf{M}_{22} = 0$ $\mathbf{M}_{31} = \mathbf{M}_{32} = 0$
Type 12	Bidirectional CPA [Bimodal]	$+$ & $-$	$+$ & $-$	$\mathbf{M}_{11} = \mathbf{M}_{12} = \mathbf{M}_{21} = \mathbf{M}_{22} = 0$
None	Unidirectional CPA from Right [+ Mode]	**None**	$+$	NOT allowed
None	Unidirectional CPA from Right [− Mode]	**None**	$-$	NOT allowed
None	Unidirectional CPA from Right [Bimodal]	**None**	$+$ & $-$	NOT allowed
None	non-CPA Action	**None**	**None**	NOT allowed

TABLE II. (Color Online) Table presents all potential CPA configurations and conditions from both sides of a TWS slab for an electromagnetic wave emitted from the left side. The symbol $\mathbf{M}_{ij}$ implies the ij component of the transfer matrix $\mathbb{M}$. The colors displayed here correspond to the CPA types that signify the reel zeros of the transfer matrix components shown in Fig. 2.

In these expressions, wave mode-specific conductivity σ_j is identified appropriately by the following quantity,

$$\sigma_j := \frac{Z_0}{2\cos\theta}\left(\sigma_{yy} + ij\sigma_{yx}\right). \tag{17}$$

Therefore, the components of the first two columns of the transfer matrix, which are crucial for defining the CPA

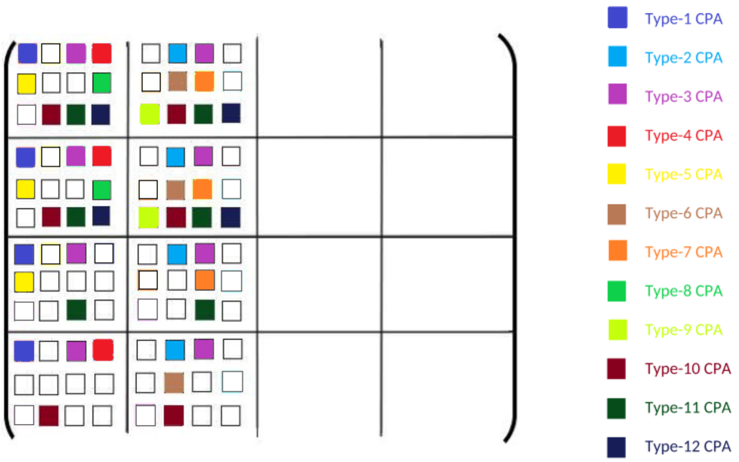

FIG. 2. (Color Online) The figure displays a diagram of TWS CPA types within the components of the transfer matrix $\mathbb{M}$ for a TWS environment. It illustrates the CPA generation conditions for each TWS CPA type listed in Table II, with different colors representing different CPA types. Notably, only the 1^{st} and 2^{nd} columns of the transfer matrix generate CPA configurations. Please note that the colors shown here correspond to the CPA types colored differently in Table II.

conditions, are determined as follows,

$$\begin{aligned}
&\mathbf{M}_{11} = \alpha^{(+)}_{+-}\, e^{-i\mathfrak{K}}, && \mathbf{M}_{12} = \beta^{(+)}_{+-}\, e^{-i\mathfrak{K}}, && \mathbf{M}_{13} = \gamma^{(+)}_{+-}\, e^{-i\mathfrak{K}}, && \mathbf{M}_{14} = \zeta^{(+)}_{+-}\, e^{-i\mathfrak{K}},\\
&\mathbf{M}_{21} = \beta^{(+)}_{-+}\, e^{-i\mathfrak{K}}, && \mathbf{M}_{22} = \alpha^{(+)}_{-+}\, e^{-i\mathfrak{K}}, && \mathbf{M}_{23} = \zeta^{(+)}_{-+}\, e^{-i\mathfrak{K}}, && \mathbf{M}_{24} = \gamma^{(+)}_{-+}\, e^{-i\mathfrak{K}},\\
&\mathbf{M}_{31} = -\gamma^{(-)}_{+-}\, e^{i\mathfrak{K}}, && \mathbf{M}_{32} = -\zeta^{(-)}_{+-}\, e^{i\mathfrak{K}}, && \mathbf{M}_{33} = -\alpha^{(-)}_{+-}\, e^{i\mathfrak{K}}, && \mathbf{M}_{34} = -\beta^{(-)}_{+-}\, e^{i\mathfrak{K}},\\
&\mathbf{M}_{41} = -\zeta^{(-)}_{-+}\, e^{i\mathfrak{K}}, && \mathbf{M}_{42} = -\gamma^{(-)}_{-+}\, e^{i\mathfrak{K}}, && \mathbf{M}_{43} = -\beta^{(-)}_{-+}\, e^{i\mathfrak{K}}, && \mathbf{M}_{44} = -\alpha^{(-)}_{-+}\, e^{i\mathfrak{K}}.
\end{aligned} \tag{18}$$

It is apparent that there are intriguing symmetries between the various components of the transfer matrix. These symmetries can be observed through the symmetry transformations applied to the indices i, j, and ℓ. Notice that $i \longleftrightarrow j$ replacement produces the symmetry between the components of the transfer matrix, $\mathbf{M}_{11} \longleftrightarrow \mathbf{M}_{22}$, $\mathbf{M}_{12} \longleftrightarrow \mathbf{M}_{21}$, $\mathbf{M}_{13} \longleftrightarrow \mathbf{M}_{24}$ and $\mathbf{M}_{14} \longleftrightarrow \mathbf{M}_{23}$ for the first two rows; $\mathbf{M}_{33} \longleftrightarrow \mathbf{M}_{44}$, $\mathbf{M}_{34} \longleftrightarrow \mathbf{M}_{43}$, $\mathbf{M}_{31} \longleftrightarrow \mathbf{M}_{42}$ and $\mathbf{M}_{32} \longleftrightarrow \mathbf{M}_{41}$ for the latter two rows. In the same way, the $\ell \to -\ell$ symmetry transformation is related to time-reversal symmetry of transfer matrix, and reveals symmetries between first and latter block pairs.

The conditions for all possible CPA types can be derived from the components of the first two columns of the transfer matrix, which we have explicitly determined. In this study, instead of analyzing each CPA type individually, we present the methods for obtaining these conditions. To demonstrate the effectiveness of the approach we have employed, we focus on two specific CPA types and provide a detailed analysis of them. These are the single-mode bidirectional CPA types generated by plus and minus mode waves incident from both sides of the TWS slab (i.e. Type 4 and Type 7 CPA configurations). The wave configurations for these CPA types are presented in Figure 3. For comparison purposes, the bimodal bidirectional wave configuration is also illustrated.

By applying the Plus and Minus mode CPA conditions (Type 4 and Type 7, respectively) presented in Table II, we obtain the following simplified self-dual spectral singularity conditions.

$$e^{2i\mathfrak{K}_\ell} = \mathbf{m}_\tau^\ell + \ell\sqrt{\mathbf{m}_\tau^{2\ell} - 1}, \tag{19}$$

where the index ℓ takes values of $+/-$ and represents the type of CPA, and the complex-valued continuous function $\mathbf{m}_\tau^\ell : \mathbb{C} \to \mathbb{C}$ is defined as follows

$$\mathbf{m}_\tau^\ell := 1 + \frac{8\mu^2\,\tilde{\mathfrak{n}}_\ell^2}{[\tilde{\mathfrak{n}}_\ell^2 - \mu^2(\sigma_\ell + 1)^2]^2}. \tag{20}$$

The subindex τ in $\mathbf{m}_\tau$ indicates that $\mathbf{m}$ is time-reversal symmetric for each ℓ. In essence, this expression is identical to those for spectral singularities that result in entirely outgoing waves. As a result, the expressions for spectral

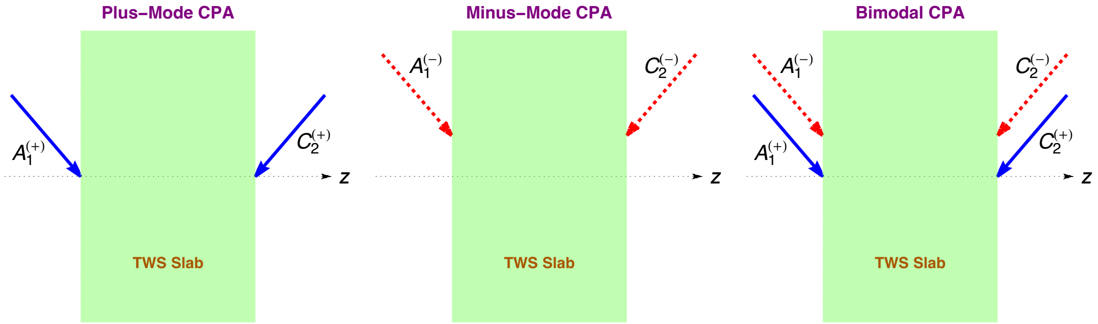

FIG. 3. (Color online) Configurations of uni- and bimodal CPA. Blue solid arrows correspond to CPA due to $\tilde{\mathfrak{n}}_+$, and red dashed arrows correspond to CPA due to $\tilde{\mathfrak{n}}_-$.

singularities and self-dual spectral singularities are fundamentally equivalent, which clarifies the concept of time-reversal symmetry. Eq. 19 plays a crucial role in controlling the CPA formation mechanism corresponding to Type 4 and Type 7 cases. Conversely, to obtain a CPA for the Type 12 case (where both the plus and minus mode waves are absorbed), the following condition must be satisfied,

$$e^{i\mathfrak{K}_\ell} = \frac{\ell(\tilde{\mathfrak{n}}_\ell - \ell\mu)^2}{\tilde{\mathfrak{n}}_\ell^2 - \mu^2}, \tag{21}$$

In the following analysis, we will focus exclusively on Type 4 and Type 7 CPA cases and highlight their notable outcomes. Consequently, we will utilize Eq. 19. For a TWS system to achieve true CPA, its parameters must satisfy this equation. The system parameters include the refractive index $\mathfrak{n}$, the TWS slab thickness L, the angle of incidence θ, the wavelength λ of the wave, and the separation b between the Weyl nodes in TWS medium. To better understand how the parameters of the TWS system are configured to support the CPA mechanism, we will investigate the role of these parameters by selecting TaAs, a material suitable for the TWS phase [30, 154–158]. The physical properties of the TaAs material we will employ are provided below [165–169].

$$\eta = 6, \qquad L = 500 \text{ nm}, \qquad b' = 5\times 10^{-4} \text{ Å}, \qquad \theta = 30^\circ, \tag{22}$$

where η is the real part of the refractive index $\mathfrak{n}$, and b' corresponds to the value of b in real physical space by $b' = 2\pi/b$. The refractive index is a complex quantity and can be expressed as the sum of its real and imaginary parts, as $\mathfrak{n} = \eta + i\kappa$. Here, η is the primary factor that determines the material type, while κ plays a crucial role in determining whether the material behaves as a gain or loss medium. For a typical material, we have $\eta \gg |\kappa|$. Since we aim to evaluate the TWS medium as a CPA, we require κ to be positive. The κ parameter can generally be related to the negative-valued loss coefficient g_l for a lossy medium. This relationship is expressed as

$$g_l := -2k\kappa. \tag{23}$$

It is essential to note that g_l must be negative for a loss-deposited medium. However, for the purpose of our graphical analysis, we will present the graphs of $g := -g_l$, as a positive value is considered more suitable for visual representation. Next, the wave vector k is related to the wavelength λ by the following equation: $k = 2\pi/\lambda$. By substituting all these parameters into the Eq. 19, we can derive the relationship between the effective parameters in the system. Our goal is to identify the optimal configuration of these parameters within the CPA formation mechanism. The most influential parameters in the system are the loss coefficient g, the wavelength λ, the incidence angle θ, and the parameter b, which reflects the primary topological character of the system. Understanding the effects of these parameters is crucial for understanding CPA mechanism.

In Figure 4, the left panel displays the locations of the self-dual spectral singularity points corresponding to the Plus mode over a broad spectrum range when $b = 0$. A similar graph can be generated for the Minus mode. The right panel illustrates the distribution of the self-dual spectral singularity points for the Plus mode when $b \neq 0$. In this case, the spectral range is confined to a narrower region, as the spectral singularity points are densely distributed, necessitating a restricted range for clearer visualization. As observed, when b is non-zero, multiple self-dual spectral singularity points occur at the same wavelength. This unexpected result arises from the topological behavior induced

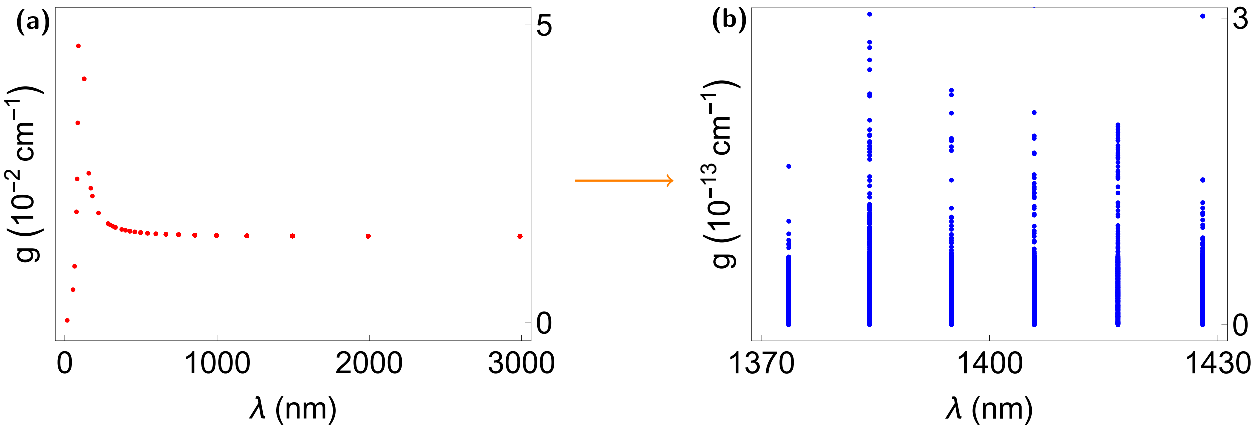

FIG. 4. (Color online) The figure illustrates the distribution of self-dual spectral singularity points in the g-lambda plane (a) in the absence of an axion term (i.e., when $b = 0$) and (b) in the presence of b-term with $b' = 5 \times 10^{-4}$ Å for Plus Mode. These points correspond to the CPA formation points. Notice that the difference between the Plus and Minus modes disappears when $b = 0$. With the inclusion of the axionic term, the topological nature of the CPA points becomes evident. These points remain topologically stable at the same lambda values. Additionally, the loss coefficients required for CPA formation decrease to substantially lower values.

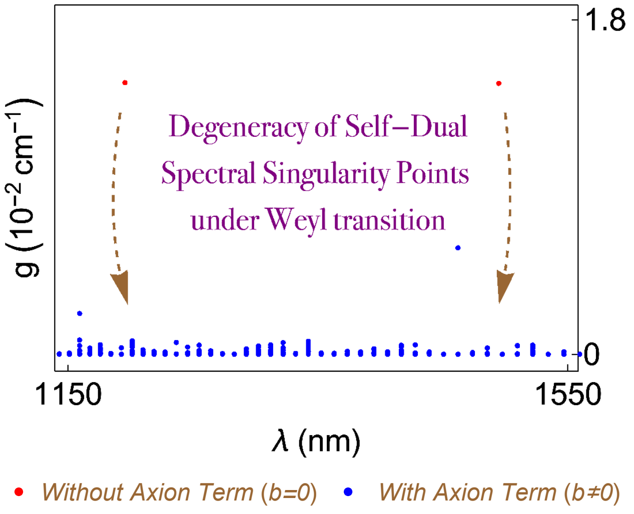

FIG. 5. (Color online) In the presence of the axion term, the self-dual spectral singularity points for the Plus Mode exhibit both topological characteristics and branch into multiple distinct points. Additionally, the threshold loss value g required for CPA formation is significantly reduced. In this graph, $b' = 5 \times 10^{-4}$ Å is used.

by the axionic content of the system. A second notable observation is the significant reduction in the loss value, indicating the potential for an efficient CPA. Finally, whereas the self-dual spectral singularity point appears at a single wavelength when $b = 0$, it manifests with topological characteristics at multiple wavelengths when b is non-zero. This surprising outcome was unexpected, and although the underlying cause of this multi-branch bands remains unclear, it is evident that it is intrinsically related to the axionic content of the system.

The multi-branch bands observed when b is non-zero is a novel and important discovery that demands detailed investigation. To explore this further, we present the graph in Fig. 5, which focuses on a narrow spectral range between 1150 nm and 1550 nm. Within this range, there are two red points, with 30 bar-shaped blue dots located between them. As observed, the increase in the number of patterns from 2 when $b = 0$ to 30 when $b \neq 0$ represents a Weyl transition, signifying the degeneracy of the self-dual spectral singularity points. When $b = 0$, both Weyl points converge and appear as a single point, causing the Weyl semimetal to behave like a Dirac semimetal. Additionally, this graph clearly demonstrates a significant reduction in the loss value, which confirms that topological materials

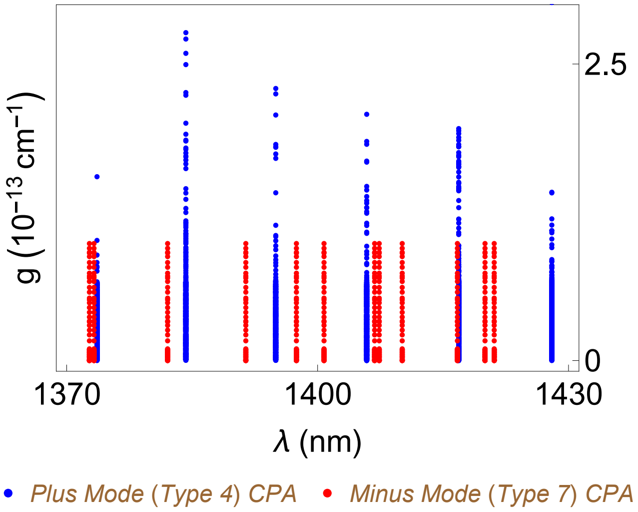

FIG. 6. (Color online) The figure shows the locations of the self-dual spectral singularity points in the λ-g plane, presented separately for the Plus and Minus modes of TWS medium. As observed, each mode exhibits distinct topological features at different wavelengths. Additionally, it is evident that the loss value is significantly reduced for both modes. Furthermore, both modes actively generate CPA at specific wavelengths, which also meet the conditions for bimodal CPA formation. In this graph, $b' = 5\times10^{-4}$ Å is used.

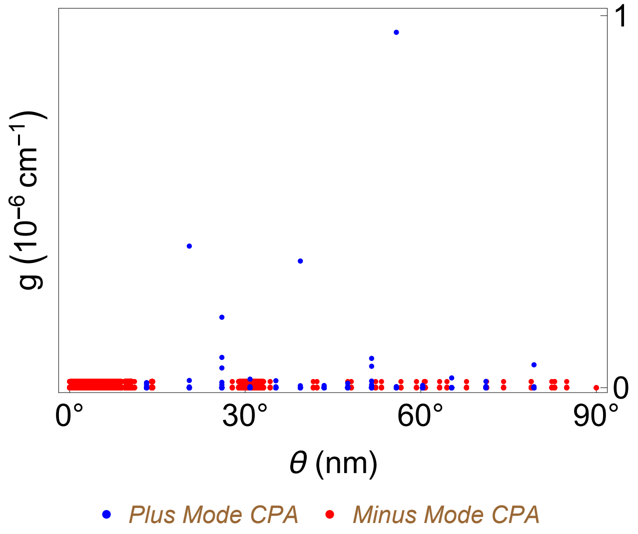

FIG. 7. (Color online) The figure depicts the placement of the self-dual spectral singularity points in the incidence angle-loss-plane for the plus and minus modes of TWS slab system. As observed, CPA formation occurs exclusively at certain angles specific to each mode. To illustrate the effect of the incident angle on the loss in the graphs, the parameter values $L = 5$ mm, $b' = 5\times10^{-4}$ Å and $\lambda = 1100$ nm were employed to enhance the visual configuration.

can be a much better CPA than regular materials because of their axionic content.

Figure 6 presents a comparison of the distributions of the self-dual spectral singularity points necessary for CPA formation in the wavelength-loss coefficient plane for both the Plus and Minus modes. As observed, the topological features associated with the band shape are clearly visible in both modes. Additionally, the wavelengths corresponding to the Plus and Minus modes differ. However, both modes are observed to occur at certain wavelengths, where the self-dual spectral singularity points can be determined using the condition in Eq. 21. These points correspond to the bimodal bidirectional CPA scenario. Finally, the loss values at the CPA points for both modes are significantly lower than those in the non-axionic case, indicating that the presence of axion content effectively reduces the loss.

Figure 7 illustrates the variation of the loss coefficient with respect to the angle of incidence for the Plus and Minus modes. As shown, CPA formation is possible only at specific angles of incidence for the given parameter values. Additionally, CPA occurs simultaneously in both modes at certain angles. Notably, CPA formation is more favorable in the Minus mode at lower angles, while the Plus mode does not exhibit CPA formation at either low or high angles. Finally, it is evident that the loss value displays a topological character as a function of the angle of incidence.

AMPLITUDE AND PHASE CONDITIONS FOR THE CPA ACTION

CPA can be viewed as an antilaser, interpreted as the time-reversed version of a laser system [66, 131–142]. Conversely, a laser system can be viewed as the time-reversed case of a CPA system, i.e., CPA $\xleftrightarrow[\text{Symmetry}]{\text{Time-Reversal}}$ Laser. Our TWS optical slab system functions as a Coherent Perfect Absorber (CPA), assuming that a time-reversed system condition is met when (self-dual) spectral singularities are present. This effect only occurs when the incoming waves possess the correct phase and amplitude. As a result, the optical system completely absorbs the incoming waves, which leads to the formation of a CPA laser. Fig. 8 visually illustrates this phenomenon.

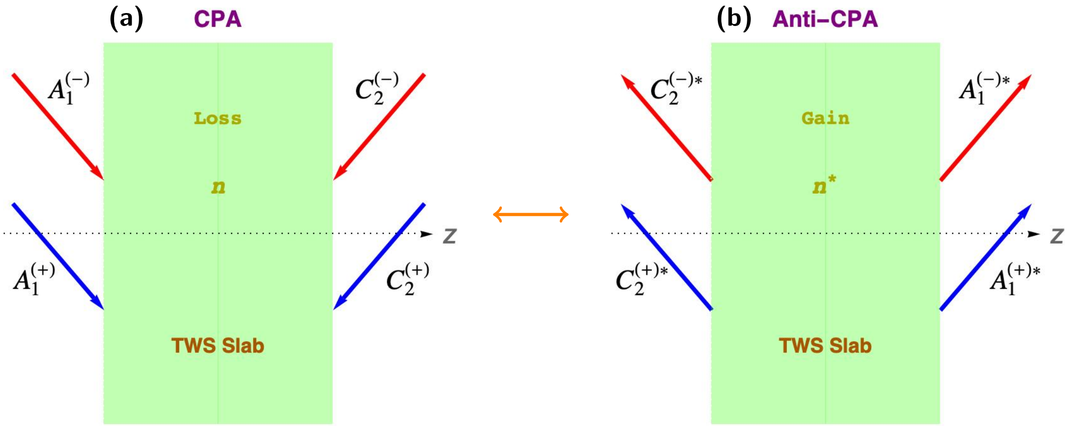

FIG. 8. (Color Online) Configurations representing the coherent perfect absorber (CPA) (Left panel) and anti-CPA (right panel). Self-dual spectral singularities correspond to purely incoming waves and anti-CPA occurs only correct phases and amplitudes of the incoming waves are appointed, which satisfy Eqs. 26 and 27.

	CPA Waves	Time Reversed Waves	Anti-CPA Waves
Leftmost Region	$A_1^{(\pm)}\, e^{i\mathfrak{K}(\mathbf{x}\tan\theta-\mathbf{z})}$	$A_1^{(\pm)*}\, e^{-i\mathfrak{K}(\mathbf{x}\tan\theta-\mathbf{z})}$	$C_2^{(\pm)*}\, e^{-i\mathfrak{K}}\, e^{-i\mathfrak{K}(\mathbf{x}\tan\theta+\mathbf{z})}$
Rightmost Region	$C_2^{(\pm)}\, e^{i\mathfrak{K}(\mathbf{x}\tan\theta+\mathbf{z})}$	$C_2^{(\pm)*}\, e^{-i\mathfrak{K}(\mathbf{x}\tan\theta+\mathbf{z})}$	$A_1^{(\pm)*}\, e^{i\mathfrak{K}}\, e^{-i\mathfrak{K}(\mathbf{x}\tan\theta-\mathbf{z})}$

TABLE III. Waves outside the TWS optical CPA slab corresponding to different phenomena specified in the first row.

The self-dual spectral singularities shown in the left panel of Fig. 8 represent purely incoming waves. The time-reversed counterpart is achieved by taking the complex conjugate of the waves outside the slab, in which case the gain component is effectively replaced instead of the loss component. In order to generate an anti-CPA laser, we reverse the incoming and outgoing waves of the time-reversed system, allowing the proper outgoing waves to be fully lased, as illustrated in the right panel of Fig. 8. Specifically, the incidence angle at $\mathbf{z} = 0$ is represented by $-\theta$ in the anti-CPA scenario, where θ is the angle that defines the CPA waves. Fig. 8 illustrates the emitted and absorbed waves as described by equations in Table III. For the necessary effect, the waves outside the active region of the optical slab are described in Table III, which uses solutions of Maxwell's equations in the external regions.

The anti-CPA laser is operational when the outcoming waves emerging at an angle θ are perfectly lased, resulting in complete destructive interference. This phenomenon can be quantified by the ratio $\rho^{(\pm)}$ corresponding to the Plus and Minus Mode configurations, respectively, which compares the complex amplitude of the incoming waves at $\mathbf{z} \to 0$

and $\mathbf{z} \to 1$. Based on the amplitudes provided in Table III, this ratio is expressed as follows:

$$\rho^{(\pm)} = \frac{C_2^{(\pm)*}\, e^{-2i\mathfrak{K}}}{A_1^{(\pm)*}}. \tag{24}$$

In fact, $C_2^{(\pm)*}$ can be expressed in terms of $A_1^{(\pm)*}$ using the self-dual spectral singularity condition for Plus/Minus modes. We recall that self-dual spectral singularities correspond to purely outgoing waves, such that

$$A_1^{(\mp)} = C_1^{(+)} = C_1^{(-)} = C_2^{(\mp)} = A_2^{(+)} = A_2^{(-)} = 0.$$

This together with the boundary conditions in Table V and self-dual spectral singularity condition in (19) leads to

$$C_2^{(\pm)} = \mathbf{M}^{(\pm)}\, A_1^{(\pm)}, \tag{25}$$

where we identified $\mathbf{M}^{(+)} := \mathbf{M}_{31}$ and $\mathbf{M}^{(-)} := \mathbf{M}_{42}$ for convenience. Therefore, it can be readily demonstrated that incoming waves corresponding to Plus and Minus modes are fully absorbed, given that the ratio of incoming amplitudes, denoted by $\rho^{(\pm)}$, satisfies the condition,

$$\rho^{(\pm)} = \mathbf{M}^{(\pm)}\, e^{-2i\mathfrak{K}}. \tag{26}$$

Therefore, the ratio of the amplitudes and the phase difference of the waves incident from the left and right are described by $|\rho|$ and $\delta\phi$, respectively, where the latter is given by

$$e^{i\delta\phi^{(\pm)}} = \frac{\rho^{(\pm)}}{\left|\rho^{(\pm)}\right|}. \tag{27}$$

As a result, CPA action can be directly achieved when the ratio of amplitudes $\left|\rho^{(\pm)}\right|$ and the phase difference $\delta\phi^{(\pm)}$ of the incoming waves from the left and right are adjusted in accordance with expressions (26) and (27), respectively. Based on the information we've gathered, we derive the following expressions for the ratio of amplitudes $\left|\rho^{(\pm)}\right|$ and the phase difference $\delta\phi^{(\pm)}$ of the incoming waves, assuming the self-dual spectral singularity condition is satisfied,

$$\left|\rho^{(\pm)}\right| = \left|\mathbf{M}^{(\pm)}\right| = \sqrt{[\mathrm{Re}\mathbf{M}^{(\pm)}]^2 + [\mathrm{Im}\mathbf{M}^{(\pm)}]^2}, \qquad \delta\phi^{(\pm)} = \tan^{-1}\left\{\frac{[\mathrm{Im}\mathbf{M}^{(\pm)}] - [\mathrm{Re}\mathbf{M}^{(\pm)}]\,\tan(2\mathfrak{K})}{[\mathrm{Re}\mathbf{M}^{(\pm)}] + [\mathrm{Im}\mathbf{M}^{(\pm)}]\,\tan(2\mathfrak{K})}\right\}. \tag{28}$$

In these expressions, the symbols Re and Im denote the real and imaginary parts of the respective quantity. Table IV presents the numerical values of the physical parameters for which different configurations of our TWS slab system function as a CPA for various incident TE waves.

	without Axion term ($b = 0$)			–	with Axion term ($b' = 5 \times 10^{-4}$ Å)		
θ	0°	−40°	−80°		0°	−40°	−80°
λ	1500.001 nm	1491.367 nm	1479.660 nm		1485.683 nm	1485.679 nm	1485.673 nm
g_ℓ	-0.01683 cm^{-1}	-0.01290 cm^{-1}	-0.00291 cm^{-1}		-1.543 cm^{-11}	-3.973 cm^{-12}	-5.024 cm^{-11}
κ	2.009×10^{-7}	1.530×10^{-7}	3.427×10^{-8}		1.825×10^{-18}	4.697×10^{-19}	5.940×10^{-18}
$\left\|\rho^{(+)}\right\|$	1.9053	1.8883	1.7817		0.5824	0.7597	1.5929
$\delta\phi^{(+)}$	146.106°	148.620°	179.940°		135.008°	135.007°	135.004°

TABLE IV. Physical parameters belonging to the construct of a (anti-) CPA for various incident angles corresponding to with and without axion cases of Plus Mode configuration. Here, TWS slab thickness is considered to be $L = 500$ nm for convenience.

AXION-INDUCED CPA CURRENTS AND THEIR TOPOLOGICAL PROPERTIES

An important aspect to consider in this context is the axion-induced current. In the current density expression derived from Maxwell's third equation, there is not only the free current but also an additional current induced by the axion term Θ, which introduces a topological feature to the system. This current is referred to as the axion-induced current and is denoted by $\vec{\mathcal{J}}_\Theta$. Its origin is rooted in the semimetallic properties of the TWS medium, and it is present both within the bulk of the material and on its surface. Thus, the presence and detection of the axion-induced current are essential for understanding the system's topological characteristics. When we examine the expression for the current density $\vec{\mathcal{J}}_\Theta$, it takes the form of a vector relation as shown below:

$$\vec{\mathcal{J}}_\Theta = -\beta\,\vec{b}\times\vec{\mathcal{E}}. \tag{29}$$

This current oscillates harmonically with time. The time-independent form of this current in a TWS loss medium can be clearly expressed as follows:

$$\vec{\mathcal{J}}_\Theta = -\frac{b\beta e^{i\mathfrak{K}\mathbf{x}\tan\theta}}{2}\left\{i(\mathcal{F}_+ - \mathcal{G}_+)\hat{e}_x + (\mathcal{F}_+ + \mathcal{G}_+)\hat{e}_y\right\}. \tag{30}$$

It is evident that this current flows within a plane perpendicular to the direction of the material's structural distribution, which is similar to the Hall current. However, the magnitude of this current is dependent on the specific conditions of each spectral singularity case corresponding to the associated laser Mode. When the relevant conditions for the Plus/Minus Mode, i.e., $A_1^{(\mp)} = C_1^{(+)} = C_1^{(-)} = C_2^{(\mp)} = A_2^{(+)} = A_2^{(-)} = 0$, are applied such that $C_2^{(\pm)} = \mathbf{M}^{(\pm)}\,A_1^{(\pm)}$ occurs. Therefore, the induced currents inside the TWS system for Plus and Minus Modes can be expressed briefly as follows:

$$\vec{\mathcal{J}}_\Theta^{(\pm)} = -b\beta A_1^{(\pm)} e^{i\mathfrak{K}(\mathbf{x}\tan\theta-1)}\mathbf{M}^{(\pm)}\left\{\left[\frac{1}{2}\cos[\mathfrak{K}_\pm(\mathbf{z}-1)] + \mathbf{a}_\pm\sin[\mathfrak{K}_\pm(\mathbf{z}-1)]\right](\hat{e}_y \pm i\hat{e}_x) - \frac{\mathbf{b}_\mp}{\sigma_\mp}\sin[\mathfrak{K}_\mp(\mathbf{z}-1)](\hat{e}_y \mp i\hat{e}_x)\right\},$$

where the coefficients $\mathbf{a}_\pm$ and $\mathbf{b}_\pm$ are given in Eq. 16. Here, $\vec{\mathcal{J}}_\Theta^{(+)}$ represents the induced current associated with the Plus Mode configuration, while $\vec{\mathcal{J}}_\Theta^{(-)}$ denotes the induced current corresponding to the Minus Mode configuration.

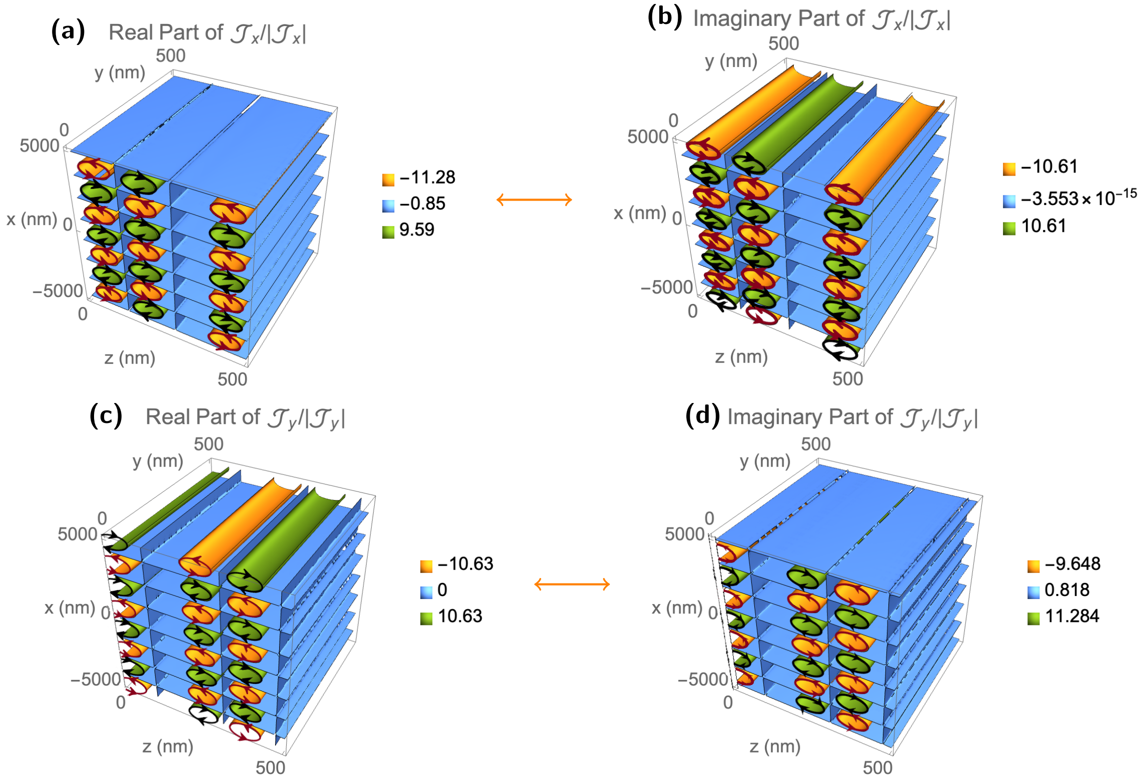

FIG. 9. (Color Online) Axion-induced currents observed in the Plus Mode self-dual spectral singularity configuration of a TWS slab. The distinct behavior of the currents in the loss region of the material is evident. The upper row shows the real and imaginary parts of the x-component of the current, while the lower row displays the behavior of the y-component. These currents, which are axion-induced Hall currents, exhibit a circular pattern.

Figures (9) and (10) present the real and imaginary parts of induced current distributions for the plus and minus mode configurations, respectively, within and on the surfaces of the TWS medium, at the moments when self-dual

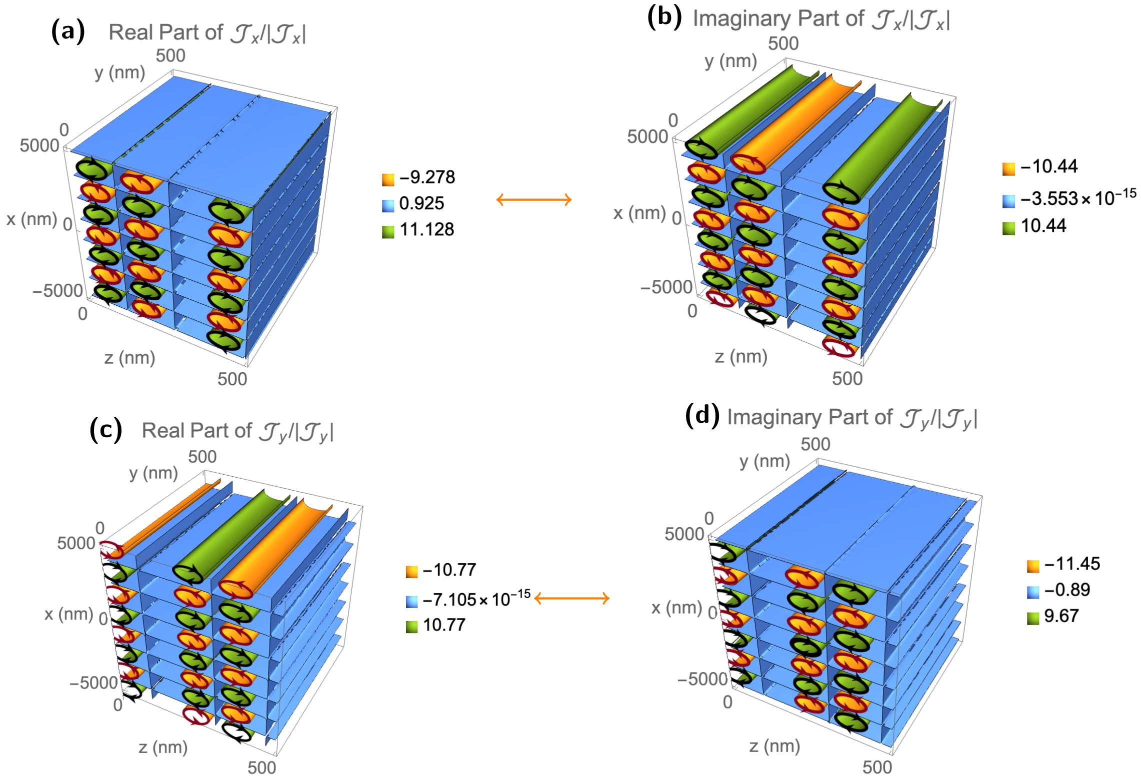

FIG. 10. (Color Online) Axion-induced currents observed at the Minus-Mode self-dual spectral singularity in a TWS slab. The currents' behavior inside the material is clearly distinguished. The upper row presents the real and imaginary components of the current along the x-axis, while the lower row shows the behavior of the current along the y-axis. These axion-driven Hall currents exhibit a circular shape.

spectral singularities arise. These current patterns are similar to those reported in Ref. [146], which supports the idea that TWS environments facilitate the formation of cyclotron-type currents due to the axion terms they contain. The self-dual spectral singularity parameters used in these plots are specified as $b' = 3$ $\mathring{A}$, $\lambda = 1405.265$, and $g = 5.763 \times 10^{-13}$ cm^{-1}. Notably, higher values of b' are chosen to obtain more distinct current distributions. As the value of b' is reduced, the number of circular patterns observed in the graphs decreases. Similarly, increasing the loss value shifts the positions of these circular patterns disorderly and anomalously along the x-axis, which is why the smallest possible loss values were utilized in this study.

From the graphs, it is evident that the axion-induced currents exhibit a fully cyclotron-like behavior, flowing in specific directions. This behavior is also an indication that the topological character of the system is preserved while the induced currents circulate in the specified directions. In other words, the existence of these currents is actually a demonstration of the topological behavior originating from the b'-term in the TWS environment. The topological symmetry here manifests itself in cyclotron-type shapes. Positive currents rotate in the clockwise direction, while negative currents rotate counterclockwise. The flow directions of these currents demonstrate a well-defined symmetry: For Plus and Minus modes, the rotations are perfectly synchronized and reversed, complementing each other. Interestingly, the rotation directions of currents in the plus mode are diametrically opposite to those in the minus mode, indicating that the plus and minus mode configurations produce contrasting current flow patterns in a lossy medium.

Lastly, these induced currents are confined to the xy-plane, while the electromagnetic wave propagates along the z-axis, thereby manifesting as a Hall current.

CONCLUDING REMARKS

In conclusion, this study presents a comprehensive analysis of Coherent Perfect Absorption (CPA) in Topological Weyl Semimetal (TWS) slabs, focusing on the unique topological properties and their impact on electromagnetic wave interactions. The study highlights the ability to achieve CPA through a carefully engineered slab geometry, where Weyl nodes are aligned along the z-axis. This configuration, coupled with the material's complex refractive index and magneto-electric effects, enables the manipulation of light through both Kerr and Faraday rotations, driven by surface currents and Fermi arcs. By applying a transfer matrix approach, the paper uncovers 12 distinct CPA types, with special attention given to Type 4 and Type 7 configurations that lead to single-mode bidirectional CPA.

Key findings reveal how material properties, such as the axion term and refractive index, play a pivotal role in reducing loss values and facilitating efficient CPA formation. The inclusion of the axion term introduces significant topological behaviors, reducing the required loss for CPA while enhancing performance under various conditions, such as varying incident angles and wavelengths. Additionally, the study explores the time-reversal symmetry between CPA and anti-CPA actions, showcasing the dual nature of these systems and their potential for creating novel laser configurations. By adjusting wave amplitudes and phases, an anti-CPA laser can be created, demonstrating the ability to reverse the absorption process, achieving perfect destructive interference and complete lasing.

The paper further delves into axion-induced currents, arising from the axion term θ, demonstrating their topological origin and behavior in TWS systems. These currents are present both in the bulk and on the surface of the material. These currents flow in the plane perpendicular to the material's structural distribution and behave similarly to a Hall current, with distinct patterns observed in the Plus and Minus Mode configurations, which show cyclotron-like motion. The current flow exhibits a topological symmetry where the directions of rotation in the Plus and Minus modes are opposite to each other, indicating contrasting current flow patterns in the lossy medium, with the currents confined to the xy-plane. These currents exhibit distinctive rotational patterns, highlighting the unique interplay between material properties and topological features that influence loss region. Overall, this research opens new avenues for the design and application of topologically engineered systems, providing a deeper understanding of CPA phenomena in TWS materials and offering exciting possibilities for light manipulation in advanced photonic devices.

Appendix

A. Modified Maxwell Equations

In the low energy limit of a TWS, spatially varying axion term plays a significant role in determining its electromagnetic response. The full action of the corresponding TWS slab system is described by the sum of conventional and axionic terms as $S = S_0 + S_\Theta$ as follows

$$S_0 = \int \left\{ -\frac{1}{4\mu_0} F_{\mu\nu} F^{\mu\nu} + \frac{1}{2} F_{\mu\nu} \mathcal{P}^{\mu\nu} - J^\mu A_\mu \right\} d^3x \, dt,$$

$$S_\Theta = \frac{\alpha}{8\pi\mu_0} \int \left\{ \Theta(\vec{r}, t) \varepsilon^{\mu\nu\alpha\beta} F_{\mu\nu} F_{\alpha\beta} \right\} d^3x \, dt,$$

where $\mathcal{P}^{\mu\nu}$ tensor represents the electric polarization and magnetization respectively by $\mathcal{P}^{0i} = cP^i$ and $\mathcal{P}^{ij} = -\varepsilon^{ijk} M_k$. Space and time dependent axion term is given by $\Theta(\vec{r}, t) = 2\vec{b} \cdot \vec{r} - 2b_0 t$, where $\vec{b}$ and b_0 denote the separation of nodes in momentum and energy space respectively. In our case, b_0 is set to be zero, since Weyl nodes are assumed to share the same chemical potential. If the action is varied with respect to A_μ, the following equations of motion is obtained

$$-\frac{1}{\mu_0} \partial_\nu F^{\mu\nu} + \partial_\nu \mathcal{P}^{\mu\nu} + \frac{\alpha}{2\pi\mu_0} \varepsilon^{\mu\nu\alpha\beta} \partial_\nu \left(\Theta F_{\alpha\beta} \right) = J^\mu \tag{31}$$

It is obvious that expanding this equation yields the modified Maxwell equations given by Eqs. 1 and 2 in the presence of axion field term.

B. Computation of Conductivities

To calculate the longitudinal σ_{yy} and transverse σ_{yx} conductivities of a TWS, we adopt the approaches given in [106**?**]. We consider the simplest case with only two nodes located at $+\vec{b}$ and $-\vec{b}$, where $\vec{b} = b\,\hat{e}_z$ in our case. Near the Weyl nodes, the linearized Hamiltonian is given by

$$H(\vec{k}) = \pm \hbar v_F \vec{\sigma} \cdot (\vec{k} \pm \vec{b}).$$

where v_F is the Fermi velocity, and $\vec{\sigma} = (\sigma_x, \sigma_y, \sigma_z)$ is the vector whose components are the Pauli matrices. Therefore, conductivity $\sigma_{\alpha\beta}$ is obtained from Kubo formula as follows

$$\sigma_{\alpha\beta}(\omega) = \frac{i}{\omega} \lim_{q\to 0} \Pi_{\alpha\beta}(q,\omega)$$

In the absence of diamagnetic term, the polarization function $\Pi_{\alpha\beta}(q,\omega)$ is given by the current-current correlation function

$$\Pi_{\alpha\beta}(q, i\omega_n) = \frac{-1}{\mathcal{V}} \int_0^\beta d\tau\, e^{i\omega_n \tau} \left\langle T_\tau \hat{\mathcal{J}}_\alpha(q,\tau) | \hat{\mathcal{J}}_\beta(-q,0) \right\rangle .$$

where $\mathcal{V}$ is the volume of the system, and the current density operator $\hat{\mathcal{J}}$ is given by

$$\hat{\mathcal{J}} = -\frac{\delta H}{\delta \vec{A}} = \pm e v_F \vec{\sigma}.$$

Once we make the analytic continuation $i\omega_n \to \omega + i0^+$, the real frequency behavior is obtained easily. Thus, for each node we obtain

$$\Pi_{\alpha\beta}(\omega) = \frac{e^2 v_F^2}{\mathcal{V}} \sum_{i,i',\vec{k}} \frac{f(\varepsilon_{i'}(\vec{k})) - f(\varepsilon_i(\vec{k}))}{\hbar\omega + \varepsilon_{i'}(\vec{k}) - \varepsilon_i(\vec{k}) + i0^+} \langle \vec{k}i|\sigma_\alpha|\vec{k}i'\rangle \langle \vec{k}i'|\sigma_\beta|\vec{k}i\rangle$$

where $f(x) = 1\big/(1+e^{\beta x})$ is the Fermi function. The expression $H(\vec{k})\,|\vec{k}i\rangle = \varepsilon_i(\vec{k})\,|\vec{k}i\rangle$ with $i = 1,2$ gives the quasiparticle energies and eigenstates. We can evaluate the longitudinal and transverse polarizations $\Pi_{\alpha\beta}(\omega)$ when Fermi energy lies with nodes. Thus, in low frequency limit, longitudinal and transverse conductivities from both nodes are found to be expressions given in (3) and (4).

C. Boundary Conditions

Boundary conditions across the surface $\mathcal{S}$ between two regions of space are given by the statements: 1) Tangential component of electric field $\vec{E}$ is continuous across the interface, $\hat{n} \times (\vec{E}_1 - \vec{E}_2) = 0$; 2) Normal component of magnetic field vector $\vec{B}$ is continuous, $\hat{n} \cdot (\vec{B}_1 - \vec{B}_2) = 0$; 3) Normal component of electric flux density vector $\vec{D}$ is discontinuous by an amount equal to the surface current density, $\hat{n} \cdot (\vec{D}_1 - \vec{D}_2) = \rho^s$; 4) Tangential component of the field $\vec{H}$ is discontinuous by an amount equal to the surface current density, $\hat{n} \times (\vec{H}_1 - \vec{H}_2) = \vec{\mathcal{J}}^s$. Here $\hat{n}$ represents the unit normal vector to the surface $\mathcal{S}$ from region 2 to region 1. In our optical configuration, we do not have the third condition since there is no normal component of electric field. Therefore, we obtain the boundary conditions as in Table V,

In this table, we used $\mathfrak{K} := k_z L$ and $\mathfrak{K}_j := \mathfrak{K}\,\tilde{\mathfrak{n}}_j$ as in Eqs. 12 and 13 . σ_j is given by Eq. 17.

---

[*] gunes.oktay@ogr.iu.edu.tr
[†] mehmetertan.indap@gmail.com
[‡] mustafa.sarisaman@istanbul.edu.tr

[1] C. Nash, "Topology and physics-a historical essay", *History of topology*, 359-415 (1999).

[2] D. S. Simon, "Topology and physics: a historical overview", in *Tying Light in Knots*, Morgan and Claypool Publishers, pp. 1-7, 2018.

[3] R. Moessner, and J. E. Moore, *Topological Phases of Matter*, Cambridge University Press, (2021).

[4] X. G. Wen, "Colloquium: Zoo of quantum-topological phases of matter", *Reviews of Modern Physics* **89(4)**, 041004 (2017).

[5] E. Witten, "Three lectures on topological phases of matter", *La Rivista del Nuovo Cimento* **39**, 313-370 (2016).

[6] B. Yan, and S. C. Zhang, "Topological materials", *Reports on Progress in Physics* **75(9)**, 096501 (2012).

[7] M. G. Vergniory, L. Elcoro, C. Felser, N. Regnault, B. A. Bernevig, and Z. Wang, "A complete catalogue of high-quality topological materials", *Nature* **566(7745)**, 480-485 (2019).

[8] B. Yan, and C. Felser, "Topological materials: Weyl semimetals", *Annual Review of Condensed Matter Physics* **8**, 337-354 (2017).

$\mathbf{z}=0$	$\sum_{j=-}^{+}\left[A_1^{(j)}+C_1^{(j)}\right]=\sum_{j=-}^{+}\left[B_1^{(j)}+B_2^{(j)}\right],$ $\sum_{j=-}^{+} j\left[A_1^{(j)}+C_1^{(j)}\right]=\sum_{j=-}^{+} j\left[B_1^{(j)}+B_2^{(j)}\right],$ $\mu\sum_{j=-}^{+} j\left[\left(1+2\sigma_j\right)A_1^{(j)}-\left(1-2\sigma_j\right)C_1^{(j)}\right]=\sum_{j=-}^{+} j\tilde{\mathfrak{n}}_j\left[B_1^{(j)}-B_2^{(j)}\right],$ $\mu\sum_{j=-}^{+}\left[A_1^{(j)}-C_1^{(j)}\right]=\sum_{j=-}^{+}\tilde{\mathfrak{n}}_j\left[B_1^{(j)}-B_2^{(j)}\right].$
$\mathbf{z}=1$	$\sum_{j=-}^{+}\left[A_2^{(j)}e^{i\mathfrak{K}}+C_2^{(j)}e^{-i\mathfrak{K}}\right]=\sum_{j=-}^{+}\left[B_1^{(j)}e^{i\mathfrak{K}_j}+B_2^{(j)}e^{-i\mathfrak{K}_j}\right],$ $\sum_{j=-}^{+} j\left[A_2^{(j)}e^{i\mathfrak{K}}+C_2^{(j)}e^{-i\mathfrak{K}}\right]=\sum_{j=-}^{+} j\left[B_1^{(j)}e^{i\mathfrak{K}_j}+B_2^{(j)}e^{-i\mathfrak{K}_j}\right],$ $\mu\sum_{j=-}^{+} j\left[\left(1+2\sigma_j\right)A_2^{(j)}e^{i\mathfrak{K}}-\left(1-2\sigma_j\right)C_2^{(j)}e^{-i\mathfrak{K}}\right]=\sum_{j=-}^{+} j\tilde{\mathfrak{n}}_j\left[B_1^{(j)}e^{i\mathfrak{K}_j}-B_2^{(j)}e^{-i\mathfrak{K}_j}\right],$ $\mu\sum_{j=-}^{+}\left[A_2^{(j)}e^{i\mathfrak{K}}-C_2^{(j)}e^{-i\mathfrak{K}}\right]=\sum_{j=-}^{+}\tilde{\mathfrak{n}}_j\left[B_1^{(j)}e^{i\mathfrak{K}_j}-B_2^{(j)}e^{-i\mathfrak{K}_j}\right].$

TABLE V. Boundary conditions for TE waves corresponding to TWS slab. Here effective indices $\tilde{\mathfrak{n}}_{\pm}$ are defined by Eq. 10.

[9] T. Zhang, Y. Jiang, Z. Song, H. Huang, Y. He, Z. Fang, H. Weng, and C. Fang, "Catalogue of topological electronic materials", *Nature* **566(7745)**, 475-479 (2019).

[10] B. J. Wieder, et al., "Topological materials discovery from crystal symmetry", *Nature Reviews Materials* **7.3**, 196-216 (2022).

[11] Y. Ando, "Topological insulator materials", *Journal of the Physical Society of Japan* **82(10)**, 102001 (2013).

[12] K. He, Y. Wang, and Q. K. Xue, "Topological materials: quantum anomalous Hall system", *Annual Review of Condensed Matter Physics* **9**, 329-344 (2018).

[13] M. Z. Hasan, and C. L. Kane, "Colloquium: topological insulators", *Reviews of modern physics* **82(4)**, 3045 (2010).

[14] M. Franz, and L. Molenkamp, *Topological insulators*, Elsevier (2013).

[15] A. Bernevig, H. Weng, Z. Fang, and X. Dai, "Recent progress in the study of topological semimetals", *Journal of the Physical Society of Japan* **87.4**, 041001 (2018).

[16] H. Gao, J. W. Venderbos, Y. Kim, and A. M. Rappe, "Topological semimetals from first principles", *Annual Review of Materials Research* **49**, 153-183 (2019).

[17] H. Weng, X. Dai, and Z. Fang, "Topological semimetals predicted from first-principles calculations", *Journal of Physics: Condensed Matter* **28(30)**, 303001 (2016).

[18] Y. B. Yang, T. Qin, D. L. Deng, L. M. Duan, and Y. Xu, "Topological amorphous metals", *Physical review letters* **123(7)**, 076401 (2019).

[19] S.-Y. Xu, et al., "Experimental discovery of a topological Weyl semimetal state in TaP", *Science advances* **1.10**, e1501092 (2015).

[20] C. Shekhar, et al., "Extremely large magnetoresistance and ultrahigh mobility in the topological Weyl semimetal candidate NbP", *Nature Physics* **11.8**, 645-649 (2015).

[21] H. Yang, et al., "Topological Weyl semimetals in the chiral antiferromagnetic materials Mn3Ge and Mn3Sn", *New Journal of Physics* **19.1**, 015008 (2017).

[22] T. M. McCormick, I. Kimchi, and N. Trivedi, "Minimal models for topological Weyl semimetals", *Physical Review B* **95.7**, 075133 (2017).

[23] I. Belopolski, et al., "Discovery of a new type of topological Weyl fermion semimetal state in MoxW1-xTe2", *Nature communications* **7.1**, 13643 (2016).

[24] M. Z. Hasan, et al., "Discovery of Weyl fermion semimetals and topological Fermi arc states", *Annual Review of Condensed Matter Physics* **8**, 289-309 (2017).

[25] P. Li, et al., "Evidence for topological type-II Weyl semimetal WTe2", *Nature communications* **8.1**, 2150 (2017).

[26] A. A. Soluyanov, et al., "Type-II Weyl semimetals", *Nature* **527.7579**, 495-498 (2015).

[27] S.-Y. Xu, et al., "Discovery of a Weyl fermion semimetal and topological Fermi arcs", *Science* **349.6248**, 613-617 (2015).

[28] H. X. Wang, et al., "Higher-order Weyl semimetals", *Physical Review Letters* **125.14**, 146401 (2020).

[29] J. Hofmann, and S. D. Sarma, "Surface plasmon polaritons in topological Weyl semimetals", *Physical Review B* **93.24**, 241402 (2016).

[30] L. X. Yang, et al., "Weyl semimetal phase in the non-centrosymmetric compound TaAs", *Nature physics* **11.9**, 728-732 (2015).

[31] N. P. Armitage, E. J. Mele, and A. Vishwanath, "Weyl and Dirac semimetals in three-dimensional solids", *Reviews of Modern Physics* **90.1**, 015001 (2018).

[32] S. Jia, S.-Y. Xu, and M. Z. Hasan, "Weyl semimetals, Fermi arcs and chiral anomalies", *Nature materials* **15.11**, 1140-1144 (2016).

[33] P. Narang, C.A.C. Garcia, and C. Felser, "The topology of electronic band structures", *Nat. Mater.* **20**, 293-300 (2021).

[34] D. Takane, Y. Kubota, K. Nakayama, et al., "Dirac semimetal phase and switching of band inversion in XMg2Bi2(XBa and Sr)", *Sci Rep* **11**, 21937 (2021).

[35] B. Singh, H. Lin, and A. Bansil, "Topology and Symmetry in Quantum Materials", *Advanced Materials* **35**, 2201058 (2023).

[36] Q. Ma, et al., "Direct optical detection of Weyl fermion chirality in a topological semimetal", *Nature Physics* **13.9**, 842-847 (2017).

[37] Y. Okamura, et al., "Giant magneto-optical responses in magnetic Weyl semimetal Co3Sn2S2", *Nature communications* **11.1**, 4619 (2020).

[38] N. Nagaosa, T. Morimoto, and Y. Tokura, "Transport, magnetic and optical properties of Weyl materials", *Nature Reviews Materials* **5.8**, 621-636 (2020).

[39] J. E. Moore, "Optical properties of Weyl semimetals", *National Science Review* **6.2**, 206-208 (2019).

[40] M. M. Jadidi, et al., "Nonlinear optical control of chiral charge pumping in a topological Weyl semimetal", *Physical Review B* **102.24**, 245123 (2020).

[41] T. Zhang, et al., "Optical Kerr effect and third harmonic generation in topological Dirac/Weyl semimetal", *Optics express* **27.26**, 38270-38280 (2019).

[42] F. Nematollahi, et al., "Topological resonance in Weyl semimetals in a circularly polarized optical pulse", *Physical Review B* **102.12**, 125413 (2020).

[43] T. Morimoto, et al., "Semiclassical theory of nonlinear magneto-optical responses with applications to topological Dirac/Weyl semimetals", *Physical Review B* **94.24**, 245121 (2016).

[44] Q. Xu, et al., "Comprehensive scan for nonmagnetic Weyl semimetals with nonlinear optical response", *npj Computational Materials* **6.1**, 32 (2020).

[45] M. I. Naher, and S. H. Naqib, "An ab-initio study on structural, elastic, electronic, bonding, thermal, and optical properties of topological Weyl semimetal TaX(X=P,As)", *Scientific Reports* **11.1**, 5592 (2021).

[46] S. Ahn, E. J. Mele, and H. Min, "Optical conductivity of multi-Weyl semimetals", *Physical Review B* **95.16**, 161112 (2017).

[47] A. Bharti, and G. Dixit, "Role of topological charges in the nonlinear optical response from Weyl semimetals", *Physical Review B* **107.22**, 224308 (2023).

[48] B. Roy, V. Juričić, and S. D. Sarma, "Universal optical conductivity of a disordered Weyl semimetal", *Scientific reports* **6.1**, 32446 (2016).

[49] V. S. Asadchy, et al., "Sub-wavelength passive optical isolators using photonic structures based on Weyl semimetals", *Advanced Optical Materials* **8.16**, 2000100 (2020).

[50] P. E. C. Ashby, and J. P. Carbotte, "Magneto-optical conductivity of Weyl semimetals", *Physical Review B* **87.24**, 245131 (2013).

[51] J. Behrends, et al., "Visualizing the chiral anomaly in Dirac and Weyl semimetals with photoemission spectroscopy", *Physical Review B* **93.7**, 075114 (2016).

[52] X. Huang, et al., "Observation of the chiral-anomaly-induced negative magnetoresistance in 3D Weyl semimetal TaAs", *Physical Review X* **5.3**, 031023 (2015).

[53] J. Behrends, et al., "Landau levels, Bardeen polynomials, and Fermi arcs in Weyl semimetals: Lattice-based approach to the chiral anomaly", *Physical Review B* **99.14**, 140201 (2019).

[54] P. E. C. Ashby, and J. P. Carbotte, "Chiral anomaly and optical absorption in Weyl semimetals", *Physical Review B* **89.24**, 245121 (2014).

[55] N. P. Ong, and S. Liang, "Experimental signatures of the chiral anomaly in Dirac–Weyl semimetals", *Nature Reviews Physics* **3.6**, 394-40 (2021).

[56] D. I Pikulin, A. Chen, and M. Franz, "Chiral anomaly from strain-induced gauge fields in Dirac and Weyl semimetals", *Physical Review X* **6.4**, 041021 (2016).

[57] E. Barnes, J. J. Heremans, and D. Minic, "Electromagnetic signatures of the chiral anomaly in Weyl semimetals", *Physical Review Letters* **117.21**, 217204 (2016).

[58] I. Belopolski, et al., "Signatures of a time-reversal symmetric Weyl semimetal with only four Weyl points", *Nature communications* **8.1**, 942 (2017).

[59] H. Weng, "Lighting up Weyl semimetals", *Nature materials* **18.5**, 428-429 (2019).

[60] C. Guo, et al., "Light control with Weyl semimetals", *Elight* **3.1**, 2 (2023).

[61] S. Wang, et al., "Quantum transport in Dirac and Weyl semimetals: a review", *Advances in Physics: X* **2.3**, 518-544 (2017).

[62] E. V. Gorbar, et al., *Electronic properties of Dirac and Weyl semimetals*, World Scientific, (2021).

[63] Y. Qi, et al., “Superconductivity in Weyl semimetal candidate MoTe2”, *Nature communications* **7.1**, 11038 (2016).

[64] C. P. Weber, “Ultrafast investigation and control of Dirac and Weyl semimetals”, *Journal of Applied Physics* **129.7**, 070901 (2021).

[65] Vetlugin, Anton N. “Coherent perfect absorption of quantum light”, *Physical Review A* **104.1**, 013716 (2021).

[66] D. G. Baranov, A. E. Krasnok, T. Shegai, A. Alù, and Y. D. Chong, “Coherent perfect absorbers: linear control of light with light”, *Nature Reviews Materials* **2**, 17064 (2017).

[67] Longhi, Stefano. “Coherent perfect absorption in a homogeneously broadened two-level medium”, *Physical Review A-Atomic, Molecular, and Optical Physics* **83.5**, 055804 (2011).

[68] Fan, Yuancheng, et al. “Tunable terahertz coherent perfect absorption in a monolayer graphene”, *Optics letters* **39.21**, 6269-6272 (2014) .

[69] Baldacci, Lorenzo, Simone Zanotto, and Alessandro Tredicucci. “Coherent perfect absorption in photonic structures”, *Rendiconti Lincei* **26**, 219-230 (2015).

[70] Wu, Zhiming, Jiahua Li, and Ying Wu. “Magnetic-field-engineered coherent perfect absorption and transmission”, *Physical Review A* **106.5**, 053525 (2022).

[71] Xiong, Wei, et al. “Coherent perfect absorption in a weakly coupled atom-cavity system”, *Physical Review A* **101.6**, 063822 (2020).

[72] Ye, Yuqian, Darrick Hay, and Zhimin Shi. “Coherent perfect absorption in chiral metamaterials”, *Optics Letters* **41.14**, 3359-3362 (2016).

[73] Yan, Chao, et al. “Coherent perfect absorption of electromagnetic wave in subwavelength structures”, *Optics and Laser Technology* **101**, 499-506 (2018).

[74] Dutta-Gupta, Shourya, et al. “Controllable coherent perfect absorption in a composite film”, *Optics express* **20.2**, 1330-1336 (2012).

[75] Zhu, Weiren, et al. “Coherent perfect absorption in an all-dielectric metasurface”, *Applied Physics Letters* **108.12**, (2016)

[76] Wu, Jin-Hui, Maurizio Artoni, and G. C. La Rocca. “Coherent perfect absorption in one-sided reflectionless media”, *Scientific Reports* **6.1**, 35356 (2016).

[77] Song, J. Z., et al. “Acoustic coherent perfect absorbers”, *New Journal of Physics* **16.3**, 033026 (2014).

[78] Yan, Dongyang, et al. “Controlling coherent perfect absorption via long-range connectivity of defects in three-dimensional zero-index media”, *Nanophotonics* **12.22**, 4195-4204 (2023).

[79] Xue, Boyi, et al. “Dual-Color Coherent Perfect Absorber”, *Physical Review Letters* **134.1**, 013802 (2025).

[80] Sun, Yong, et al. “Experimental demonstration of a coherent perfect absorber with PT phase transition”, *Physical review letters* **112.14**, 143903 (2014).

[81] Yan, Xiao-Bo, et al. “Coherent perfect absorption, transmission, and synthesis in a double-cavity optomechanical system”, *Optics Express* **22.5**, 4886-4895 (2014).

[82] Hörner, Helmut, et al. “Coherent perfect absorption of arbitrary wavefronts at an exceptional point”, *Physical Review Letters* **133.17**, 173801 (2024).

[83] Müllers, Andreas, et al. “Coherent perfect absorption of nonlinear matter waves”, *Science Advances* **4.8**, eaat6539 (2018).

[84] Suwunnarat, Suwun, et al. “Non-linear coherent perfect absorption in the proximity of exceptional points”, *Communications Physics* **5.1**, 5 (2022).

[85] Villinger, Massimo L., et al. “Analytical model for coherent perfect absorption in one-dimensional photonic structures”, *Optics letters* **40.23**, 5550-5553 (2015).

[86] Wang, Cheng-Zhen, et al. “Nonlinearity-induced scattering zero degeneracies for spectral management of coherent perfect absorption in complex systems”, *Physical Review Applied* **22.6**, 064093 (2024).

[87] Nie, Guangyu, et al. “Selective coherent perfect absorption in metamaterials”, *Applied Physics Letters* **105.20**, (2014).

[88] del Hougne, Philipp, et al. “On-demand coherent perfect absorption in complex scattering systems: time delay divergence and enhanced sensitivity to perturbations.”*Laser and Photonics Reviews* **15.7**, 2000471 (2021).

[89] Konotop, Vladimir V., and Dmitry A. Zezyulin. “Linear and nonlinear coherent perfect absorbers on simple layers”, *Physical Review A* **97.6**, 063850 (2018).

[90] Li, Ying, and Christos Argyropoulos. “Tunable nonlinear coherent perfect absorption with epsilon-near-zero plasmonic waveguides”, *Optics letters* **43.8**, 1806-1809 (2018).

[91] Wei, Pengjiang, et al. “Symmetrical and anti-symmetrical coherent perfect absorption for acoustic waves”, *Applied Physics Letters* **104.12**, (2014).

[92] Guo, Miaodi, et al. “Tunable nonlinear coherent perfect absorption in cavity QED”, *Physical Review A* **107.3**, 033704 (2023).

[93] Dutta-Gupta, Shourya, et al. “Coherent perfect absorption mediated anomalous reflection and refraction”, *Optics letters* **37.21**, 4452-4454 (2012).

[94] Bai, Ping, Ying Wu, and Yun Lai. “Multi-channel coherent perfect absorbers”, *Europhysics Letters* **114.2**, 28003 (2016).

[95] Lan, Guilian, et al. “Dynamically tunable coherent perfect absorption in topological insulators at oblique incidence”, *Optics Express* **29.18**, 28652-28663 (2021).

[96] Park, Chan Young, et al. “Compact coherent perfect absorbers using topological guided-mode resonances”, *Scientific Reports* **14.1**, 14144 (2024).

[97] Wu, Jipeng, et al. “Tunable coherent perfect absorption in three-dimensional Dirac semimetal films”, *Chinese Optics Letters* **19.8**, 081601 (2021).

[98] Zhou, Ting, et al. “Dynamically tunable coherent perfect absorption based on bulk Dirac semimetal”, *Journal of the Optical Society of America B* **37.7**, 1987-1995 (2020).

[99] Sarısaman, Mustafa, and Murat Tas. "Broadband coherent perfect absorber with PT-symmetric 2D-materials", *Annals of Physics* **401**, 139-148 (2019).

[100] Kang, Wenjing, et al. "Dual-controlled tunable terahertz coherent perfect absorption using Dirac semimetal and vanadium dioxide", *Results in Physics* **19**, 103688 (2020).

[101] Tang, Kezheng, et al. "Dynamically tunable coherent perfect absorption and transparency in Dirac semimetal metasurface", *Optical Materials Express* **9.9**, 3649-3656 (2019).

[102] Lan, Guilian, et al. "Dynamically tunable coherent perfect absorption in topological insulators at oblique incidence", *Optics Express* **29.18**, 28652-28663 (2021).

[103] F. Wilczek, "Two applications of axion electrodynamics", *Physical review letters* **58.18**, 1799 (1987).

[104] A. Sekine, and K. Nomura, "Axion electrodynamics in topological materials", *Journal of Applied Physics* **129.14**, 141101 (2021).

[105] J. Planelles, "Axion electrodynamics in topological insulators for beginners", *arXiv preprint* arXiv:2111.07290 (2021).

[106] M. Kargarian, M. Randeria, and N. Trivedi, "Theory of Kerr and Faraday rotations and linear dichroism in Topological Weyl Semimetals", *Scientific Reports* **5**, 12683 (2015).

[107] C. M. Bender, and S. Boettcher. "Real spectra in non-Hermitian Hamiltonians having P T symmetry", *Physical review letters* **80.24**, 5243 (1998).

[108] R. El-Ganainy, et al., "Non-Hermitian physics and PT symmetry", *Nature Physics* **14.1**, 11-19 (2018).

[109] K. G. Makris, R. El-Ganainy, D. N. Christodoulides, and Z. H. Musslimani, "Beam Dynamics in PT Symmetric Optical Lattices", *Phys. Rev. Lett.* **100**, 103904 (2008).

[110] A. Mostafazadeh, "Pseudo-Hermitian representation of quantum mechanics", *Int. J. Geom. Meth. Mod. Phys.* **7**, 1191 (2010); C. M. Bender, D. C. Brody, and H. F. Jones, "Must a hamiltonian be hermitian?", *Am. J. Phys.* **71**, 1095 (2003).

[111] S. Longhi, "Invisibility in non-Hermitian tight-binding lattices", *Phys. Rev. A* **82**, 032111 (2010).

[112] S. Longhi, "Invisibility in-symmetric complex crystals", *J. Phys. A* **44**, 485302 (2011).

[113] Y. Ashida, Z. Gong, and M. Ueda, "Non-hermitian physics", *Advances in Physics* **69.3**, 249-435 (2020).

[114] K. Kawabata, et al., "Symmetry and topology in non-Hermitian physics", *Physical Review X* **9.4**, 041015 (2019).

[115] N. Okuma, and M. Sato. "Non-Hermitian topological phenomena: A review", *Annual Review of Condensed Matter Physics* **14**, 83-107 (2023).

[116] H. Wang, et al., "Topological physics of non-Hermitian optics and photonics: a review", *Journal of Optics* **23.12**, 123001 (2021).

[117] E. J. Bergholtz, J. C. Budich, and F. K. Kunst, "Exceptional topology of non-Hermitian systems", *Reviews of Modern Physics* **93.1**, 015005 (2021).

[118] C. M. Bender, "Making sense of non-Hermitian Hamiltonians", *Reports on Progress in Physics* **70.6**, 947 (2007).

[119] M. A. Bandres, and M. Segev, "Non-Hermitian topological systems", *Physics* **11**, 96 (2018).

[120] K. Ding, C. Fang, and G. Ma, "Non-Hermitian topology and exceptional-point geometries", *Nature Reviews Physics* **4.12**, 745-760 (2022).

[121] N. Moiseyev, *Non-Hermitian quantum mechanics*, Cambridge University Press, (2011).

[122] A. Ghatak, and T. Das, "New topological invariants in non-Hermitian systems", *Journal of Physics: Condensed Matter* **31.26**, 263001 (2019).

[123] V. M. M. Alvarez, et al., "Topological states of non-Hermitian systems", *The European Physical Journal Special Topics* **227**, 1295-1308 (2018).

[124] Z. Gong, et al., "Topological phases of non-Hermitian systems", *Physical Review X* **8.3**, 031079 (2018).

[125] A. Mostafazadeh, "Invisibility and PT symmetry", *Phys. Rev. A* **87**, 012103 (2013).

[126] G. Oktay, M. Sarısaman, and M. Tas, "Lasing with Topological Weyl Semimetal", *Scientific Reports* **10**, 3127 (2020).

[127] A. Mostafazadeh, M. Sarısaman, "Spectral singularities of a complex spherical barrier potential and their optical realization", *Phys. Lett. A* **375**, 3387 (2011); "Optical spectral singularities and coherent perfect absorption in a two-layer spherical medium", *Proc. R. Soc. Lond. Ser. A Math. Phys. Eng. Sci.* **468**, 3224 (2012); "Spectral singularities and whispering gallery modes of a cylindrical gain medium", *Phys. Rev. A* **87**, 063834 (2013); "Spectral singularities in the surface modes of a spherical gain medium", *Phys. Rev. A* **88**, 033810 (2013); "Lasing-threshold condition for oblique TE and TM modes, spectral singularities, and coherent perfect absorption", *Phys. Rev. A* **91**, 043804 (2015).

[128] A. Mostafazadeh and M. Sarısaman, "Spectral singularities in the TE and TM modes of a PT-symmetric slab system: Optimal conditions for realizing a CPA-laser", *Ann. Phys. (NY)* **375**, 265-287 (2016).

[129] M. Sarisaman and M. Tas, "PT-symmetric coherent perfect absorber with graphene", *J. Opt. Soc. Am. B* **35**, 2423 (2018).

[130] A. Mostafazadeh, "Optical spectral singularities as threshold resonances", *Phys. Rev. A* **83.4**, 045801 (2011).

[131] Y. D. Chong, L. Ge, H. Cao, and A. D. Stone, "Coherent perfect absorbers: time-reversed lasers", *Phys. Rev. Lett.* **105**, 053901 (2010).

[132] S. Longhi, "Backward lasing yields a perfect absorber", *Physics* **3**, 61 (2010).

[133] S. Longhi, "PT-symmetric laser absorber", *Phys. Rev. A* **82**, 031801 (2010).

[134] S. Longhi, "Coherent perfect absorption in a homogeneously broadened two-level medium", *Phys. Rev. A* **83**, 055804 (2011).

[135] S. Longhi, "Time-reversed optical parametric oscillation", *Phys. Rev. Lett.* **107**, 033901 (2011).

[136] W. Wan, Y. Chong, L. Ge, H. Noh, A. D. Stone, and H. Cao, "Time-reversed lasing and interferometric control of absorption", *Science* **331**, 889 (2011).

[137] L. Ge, Y. D. Chong, S. Rotter, H. E. Türeci, and A. D. Stone, "Unconventional modes in lasers with spatially varying gain and loss", *Phys. Rev. A* **84**, 023820 (2011).

[138] Pichler, Kevin, et al. “Random anti-lasing through coherent perfect absorption in a disordered medium”, *Nature* **567.7748**, 351-355 (2019).

[139] Bai, Ping, et al. “Simultaneous realization of a coherent perfect absorber and laser by zero-index media with both gain and loss”, *Physical review A* **94.6**, 063841 (2016).

[140] Fu, Yangyang, et al. “Coherent perfect absorption and laser modes in a cylindrical structure of conjugate metamaterials”, *New Journal of Physics* **20.1**, 013015 (2018).

[141] Fu, Yangyang, et al. “Coherent perfect absorber and laser modes in purely imaginary metamaterials”, *Physical Review A* **96.4**, 043838 (2017).

[142] Yang, Minye, et al. “Experimental observation of coherent-perfect-absorber and laser points in anti-PT symmetry”, *Physical Review A* **110.3**, 033504 (2024).

[143] A. Mostafazadeh, “Spectral Singularities of Complex Scattering Potentials and Infinite Reflection and Transmission Coefficients at Real Energies”, *Phys. Rev. Lett.* **102**, 220402 (2009).

[144] M. Sarısaman, “Unidirectional reflectionlessness and invisibility in the TE and TM modes of a PT-symmetric slab system”, *Phys. Rev. A* **95**, 013806 (2017).

[145] M. Sarısaman and M. Tas, “Unidirectional invisibility and PT symmetry with graphene”, *Phys. Rev. B* **97**, 045409 (2018).

[146] M. Sarisaman, S. Tasdemir, and S. Rostamzadeh, “Topological behavior of spectral singularities in topological Weyl semimetals”, *Journal of Physics: Condensed Matter* **36.40**, 405603 (2024).

[147] H. Ghaemi-Dizicheh, A. Mostafazadeh, and M. Sarısaman, “Spectral singularities and tunable slab lasers with 2D material coating”, *JOSA B* **37.7**, 2128-2138 (2020).

[148] M. Sarısaman, and M. Tas, “Broadband and wide-angle invisibility with PT-symmetric 2D-Weyl semimetal”, *Journal of Applied Physics* **126.16**, 163102 (2019).

[149] M. Sarısaman et al., “Energy Stored in a Slab Covered by Graphene Sheets”, in *Carbon Related Materials: Commemoration for Nobel Laureate Professor Suzuki Special Symposium at IUMRS-ICAM2017*, Springer, Singapore, (2021).

[150] H. Alomeare, F. Nutku, and M. Sarısaman, “Circular dichroism in nonlinear topological Weyl semimetals”, *Journal of Optics* **26.6**, 065502 (2024).

[151] A. Mostafazadeh, “Self-dual spectral singularities and coherent perfect absorbing lasers without $\mathcal{PT}$-symmetry”, *J. Phys. A* **45**, 444024 (2012).

[152] M. A. Naimark, “On Spectral Theory,” Trudy Moscov. Mat. Obsc. **3**, 181 (1954) (in Russian); Engl. transl.: Amer. Math. Soc. Transl. (2) **16**, 103 (1960). For a list of mathematical literature on spectral singularities, see G. Sh. Guseinov, Pramana J. Phys. **73**, 587 (2009) and [153].

[153] A. Mostafazadeh, “Geometric Methods in Physics,” in *Trends in Mathematics*, edited by P. Kielanowski, P. Bieliavsky, A. Odzijewicz, M. Schlichenmaier, and T. Voronov (Springer, Cham, 2015), pp. 145-165; arXiv:1412.0454.

[154] B. Q. Lv, H. M. Weng, B. B. Fu, X. P. Wang, H. Miao, J. Ma, P. Richard, X. C. Huang, L. X. Zhao, G. F. Chen, Z. Fang, X. Dai, T. Qian, and H. Ding, *Phys. Rev. X* **5**, 031013 (2015).

[155] S. -M. Huang, S. -Y. Xu, I. Belopolski, C. -C. Lee, G. Chang, B. Wang, N. Alidoust, G. Bian, M. Neupane, C. Zhang, S. Jia, A. Bansil, H. Lin, and M. Z. Hasan, *Nat. Commun.* **6.1**, 7373 (2015).

[156] B. Xu, et al., “Optical spectroscopy of the Weyl semimetal TaAs”, *Physical Review B* **93.12**, 121110 (2016).

[157] Z. Li, et al., “Weyl semimetal TaAs: crystal growth, morphology, and thermodynamics”, *Crystal Growth and Design* **16.3**, 1172-1175 (2016).

[158] B. Q. Lv, et al., “Observation of Weyl nodes in TaAs”, *Nature Physics* **11.9**, 724-727 (2015).

[159] Q. Chen, et al., “Optical properties and electromagnetic modes of Weyl semimetals”, *Physical Review B* **99.7**, 075137 (2019).

[160] Y. Gao, et al., “Chiral terahertz wave emission from the Weyl semimetal TaAs”, *Nature communications* **11.1**, 720 (2020).

[161] Y. Ye, et al., “Tunable mid-infrared refractive index sensor with high angular sensitivity and ultra-high figure-of-merit based on Dirac semimetal”, *Results in Physics* **17**, 103035 (2020).

[162] X. -G. Wan, A. M. Turner, A. Vishwanath, and S. Y. Savrasov, *Phys. Rev. B* **83**, 205101 (2011); G. Xu, H. Weng, Z. Wang, X. Dai, and Z. Fang, *Phys. Rev. Lett.* **107**, 186806 (2011); A. A. Burkov and L. Balents, *Phys. Rev. Lett.* **107**, 127205 (2011); L. Lu, L. Fu, J. D. Joannopoulos, and M. Soljačić, *Nat. Photon.* **7**, 294 (2013).

[163] S. -Y. Xu, I. Belopolski, N. Alidoust, M. Neupane, G. Bian, C. Zhang, R. Sankar, G. Chang, Z. Yuan, C. -C. Lee, S. -M. Huang, H. Zheng, J. Ma, D. S. Sanchez, B. Wang, A. Bansil, F. Chou, P. P. Shibayev, H. Lin, S. Jia, and M. Z. Hasan, *Science* **349**, 613 (2015).

[164] J. Ruan, S. -K. Jian, H. Yao, H. Zhang, S. -C. Zhang, and D. Xing, *Nat. Commun.* **7**, 11136 (2016); X. Huang, L. Zhao, Y. Long, P. Wang, D. Chen, Z. Yang, H. Liang, M. Xue, H. Weng, Z. Fang, X. Dai, and G. Chen, *Phys. Rev. X* **5**, 031023 (2015); C. -L. Zhang et al., *Nat. Commun.* **7**, 10735 (2016).

[165] J. Buckeridge, D. Jevdokimovs, C. R. A. Catlow, and A. A. Sokol, “Bulk electronic, elastic, structural, and dielectric properties of the Weyl semimetal TaAs”,*Phys. Rev. B* **93**, 125205 (2016).

[166] B. J. Ramshaw, K. A. Modic, A. Shekhter, Y. Zhang, E. Kim, P. J. W. Moll, M. D. Bachmann, M. K. Chan, J. B. Betts, F. Balakirev, A. Migliori, N. J. Ghimire, E. D. Bauer, F. Ronning and R. D. McDonald, “Quantum limit transport and destruction of the Weyl nodes in TaAs”, *Nature Comm.* **9**, 2217 (2018).

[167] M. Dadsetani, A. Ebrahimian, “Optical Distinctions Between Weyl Semimetal TaAs and Dirac Semimetal Na_3Bi: An Ab Initio Investigation”, *Journal of Elec. Mater.* **45**, 5867 (2016).

[168] W. T. Silfvast, *Laser Fundamentals*, Cambridge University Press, Cambridge, (1996).

[169] I. Kriegel, M. Guizzardi, F. Scotognella, “Tantalum Arsenide-Based One-Dimensional Photonic Structures”, *Ceramics* **1**(1), 139-144 (2018).